Abundances of iron-peak elements in disk and bulge giant stars from high-resolution optical spectra

Maria Lomaeva

Lund Observatory
Lund University

2018-EXA133

Degree project of 60 higher education credits (for a degree of Master)
May 2018

Supervisors: Nils Ryde and Henrik Jönsson

Lund Observatory
Box 43
SE-221 00 Lund
Sweden

Abstract

Context. The formation and evolution of the Galactic bulge and the Milky Way is still a debated subject. Observations of, e.g., the X-shaped bulge, cylindrical stellar motions and young stars in the bulge have suggested that the bulge formed through secular evolution of the disk and not through gas dissipation and/or mergers, as thought previously.
Data. We use high-resolution optical spectra of 291 K giants in the local disk obtained by the FIES spectrograph on the Nordic Optical Telescope (S/N = 80-100 for most of the disk spectra) and 46 K giants in the bulge obtained by the UVES/FLAMES spectrograph on the ESO Very Large Telescope (S/N = 10-80).
Aims. The goal of this work is to examine stellar samples from the thin and thick disk as well as the bulge and measure abundances of six iron-peak elements (Sc, V, Cr, Mn, Co and Ni). These can provide additional observational constraints for Galaxy formation and chemical evolution models and help to understand whether the bulge has emerged from the (thick) disk or not.
Methods. We determine the abundances in the Solar neighbourhood and bulge by synthesising line profiles using the programme Spectroscopy Made Easy (SME) and 1-D, spherically-symmetric MARCS model atmospheres under the assumption of local thermodynamic equilibrium (LTE). We also separate the thin and thick disk stellar populations according to their [Ti/Fe]-ratios and radial velocities using a Gaussian Mixture Model (GMM). Moreover, we apply NLTE corrections for Co as well.
Results. The [(Sc,V,Co)/Fe] vs. [Fe/H] trends show a clear separation between the disk components, being more enhanced in the thick disk. The same is observed for Ni but to a lesser extent. The trends of Sc, V and Co are also more enhanced in the bulge compared to the thick disk, whereas the [Ni/Fe] ratio is similar in the thick disk and the bulge. Our [Mn/Fe] ratio steadily increases with increasing metallicity at about the same rate in all the three components. For Cr, we find a flat trend around [Cr/Fe] $\sim$0 for the whole metallicity range in the disk and the bulge. We also observe a higher average metallicity in the bulge compared to the disk.
Conclusions. The significantly enhanced [(Sc,V,Co)/Fe] ratios that we determine from our data of stars in the bulge, suggest that the local thick disk and the bulge have experienced different chemical enrichment and evolutionary paths. However, we are unable to predict the exact evolutionary path of the bulge solely based on these observations. Galactic chemical evolution models could, on the other hand, provide that using these results.

Populärvetenskaplig beskrivning

Solen och alla stjärnor som vi ser på natthimlen tillhör vår Galax - Vintergatan. Vintergatan är en spiralgalax med en utbuktning i dess centrum - bulben. För att förstå hur Vintergatan blev till måste man ha en bra uppfattning om bulbens ursprung. Under många år trodde vi att vi visste hur bulben och hela Galaxen hade formats, men ny teknologi, förbättrade teleskop och instrument samt simuleringar av galaxutvecklingen har visat oss att det inte var fallet. Förut trodde man att bulben formades våldsamt och snabbare än galaxskivan genom att gas föll in och formade ett sfäriskt klot. I detta fall skulle bulben sakna unga stjärnor, och stjärnorna skulle röra sig med slumpmässiga banor runt Galaxcentrum. Nya observationer har dock visat att bulben snarare är formad som ett "X", att det finns en del mycket unga stjärnor, och att stjärnor rör sig som om de befinner sig i en osynlig cylinder. Allt detta tyder snarare på att bulben förmodligen uppstod från galaxskivan vid en dynamisk instabilitet som fick den att bukta ut i mitten.

Förutom stjärnornas åldrar, rörelser och formen på bulben, kan man även studera deras kemiska sammansättning för att få fler ledtrådar. Om bulben uppstod snabbt och oberoende av galaxskivan så kommer även stjärnornas sammansättning att skilja sig avsevärt i dessa delar av Vintergatan. En av svårigheterna med observationer av Vintergatans mitt är att den ligger långt bort från oss på ett avstånd som motsvarar ca 26 000 ljusår. Därför måste stjärnor som man observerar vara tillräckligt ljusstarka. Av denna anledning, är röda jättestjärnor (K-jättar) ett passande alternativ eftersom de är väldigt luminösa tack vare deras storlek. Dessutom lever de relativt länge och därför bevarar de informationen om den unga Vintergatan i sina grundämneshalter.

I vårt arbete, mäter vi halter av sex grundämnen som tillhör den så kallade "järntoppen" i periodiska systemet: skandium (Sc), vanadium (V), krom (Cr), mangan (Mn), kobolt (Co) och nickel (Ni). Dessa grundämnen bildas i exploderande massiva stjärnor och vita dvärgar. Vi använder oss av högupplösta observerade spektra av 291 K-jättar i solens närhet samt 46 K-jättar i bulben. För att få fram halter, jämför vi observerade spektra med syntetiskt framtagna spektra som skapas utifrån modelatmosfärer med hjälp av atomdata. Eftersom diskstjärnorna har visat sig tillhöra två olika grupper, tunn och tjock disk, separerar vi dem beroende på deras kinematik och kemisk sammansättning av titan för mer homogen analys.

Genom att studera halttrender av "järntopp"-grundämnen i galaxskivan och bulben, ser vi att trender som tillhör Sc, V och Co samt även Ni, till en mindre grad, är mer förhöjda i tjocka disken jämfört med tunna. Halterna av Sc, V och Co är ännu högre i bulben än i tjocka disken, medan Ni ligger på ungefär samma nivå i dessa två Galaktiska komponenter. Disk- och bulbtrenderna för Mn överlappar varandra helt och har liknande stigande lutning. Cr-trenderna är platta både i bulben och disken. Skillnaderna i Sc, V och Co i bulben och tjocka disken leder oss till slutsatsen att utvecklingen i dessa områden kan ha varit (något) annorlunda. Förmodligen har stjärnbildningen varit snabbare i bulben. Nu kan, alltså, vår data användas för att säga något om bulbens utveckling. Genom att modellera våra halttrender kan s.k. galaktiska kemiska utvecklingsmodeller sätta starkare villkor på händelseförloppen som ledde till bildandet och utvecklingen av bulben.

Acknowledgements

I would like to express my deep gratitude to my supervisors Nils Ryde and Henrik Jönsson for their continuous support of my Master's studies. I am very grateful for their time, patience and motivation. Their "open-door policy" and willingness to share their expertise have helped me to improve my knowledge in optical stellar spectroscopy greatly.

I would also like to thank Brian Thorsbro and other members of the LISA group for helpful discussions concerning my thesis and stellar spectroscopy in general.

Contents

List of Figures

List of Tables

Chapter 1

Introduction

One of the most important questions in contemporary astrophysics concerns the formation and evolution of galaxies (Bland-Hawthorn & Gerhard 2016). The Milky Way is a typical barred spiral galaxy and is the only galaxy where we can resolve individual stars for a detailed analysis. This provides a great deal of knowledge about its evolutionary path. Ultimately, understanding how the Milky Way has formed and evolved will also improve our understanding of spiral galaxies in general.

The flattened stellar disk(s) concentrated on the Galactic midplane dominate the appearance of the Milky Way. Several studies have shown that there are two distinct stellar populations present in the local disk: thin and thick disk populations. Members of the latter group tend to have lower rotational velocities around the Galactic centre, hotter kinematics and higher ages and abundances of α-elements at a given metallicity on average compared to the stars from the thin disk (e.g. Bensby et al. 2007, 2014; Adibekyan et al. 2011). Surrounding the centre lies a high stellar density region, the bulge. A schematic view of these Galactic components is shown in Figure 1.1.

To fully understand the formation of the Galaxy, it is essential to understand the formation of the bulge. The bulge is a major Galactic component contributing to a significant fraction of the total stellar mass in the Milky Way[1]. In the early studies, the common perception of the bulge was based on the idea that it resembles elliptical galaxies (e.g. McWilliam 2016, Kormendy 2016), i.e., it was thought that the bulge was spherical, gas depleted, and that its stars were predominantly old with metal-rich stars having non-solar scaled element mixtures (cf. Henry & Worthey 1999; Kobayashi & Arimoto 1999) with random orbital motions. The bulge was also expected to have a clear radial metallicity gradient due to a fast star-formation history (Pipino & Matteucci 2008). The aforementioned properties

[1] E.g., $M_{*,bulge} = 2.0 \pm 0.3 \cdot 10^{10} M_{\odot}$ (Valenti et al. 2016); $M_{*,total} = 6.43 \pm 0.63 \cdot 10^{10} M_{\odot}$ (McMillan 2011)

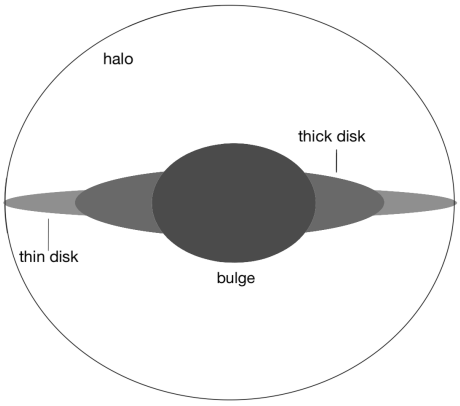

Figure 1.1: A schematic view of the Milky Way: the halo, bulge, thin and thick disk components are indicated.

would place the bulge into the group of so-called classical bulges (Kormendy & Kennicutt 2004a).

Classical bulges form fast in the early stages of galaxy formation through dissipative collapse of the primordial gas cloud or hierarchical growth through mergers according to the ΛCDM theory (e.g. Abadi et al. 2003; Scannapieco & Tissera 2003). Various dissipative collapse models have proposed one or more gas accretion events, where each accretion event forms the halo/bulge, the thick and eventually the thin disk (Eggen et al. 1962; Chiappini et al. 1997; Micali et al. 2013). Such formation occurs "inside-out", despite the similarities between classical bulges and elliptical galaxies, where the latter form "outside-in" converting the gas into stars in the outermost regions faster than in the core (Pipino & Matteucci 2008).

However, several recent observations of the Milky Way bulge have challenged this picture. E.g., the revelation of an X-shape of the bulge rather than spherical contradicted the classical bulge models and placed the Galactic bulge into the group of dynamically formed bulges with a boxy/peanut (b/p) structure which represents the inner, 3-D part of the Galactic bar (McWilliam & Zoccali 2010; Nataf et al. 2010; Wegg & Gerhard 2013). The b/p structure has also been seen in many other spiral galaxies (Lütticke et al. 2000; Kormendy & Kennicutt 2004b). Several N-body simulations of the evolution of spiral galaxies have managed to reproduce the b/p bulge shape through secular disk instabilities (e.g., Combes & Sanders 1981; Athanassoula 2005; Martinez-Valpuesta et al. 2006). In such simulations, stellar bars experience one or even multiple buckling instabilities which result in a boxy or peanut-shaped structure depending on the viewing angle (e.g. Di Matteo

et al. 2014).

Furthermore, the observed metallicity gradient in the bulge has been used as evidence for the classical bulge case; moreover, the vertical gradient was thought to be erased by bars mixing the stellar orbits, opposing the secular evolution scenario (Gonzalez & Gadotti 2016). Interestingly, bar formation models of disk galaxies have shown that a similar gradient can be reproduced with the presence of a bar (e.g., Di Matteo et al. 2014). Additionally, the metallicity gradient can also suggest that several stellar populations with distinct metallicities are present in the bulge: e.g., two, as found in Hill et al. (2011) or three, as in Ness et al. (2013a)[2].

The observed cylindrical rotation of the bulge stars from the BRAVA (Kunder et al. 2012) and ARGOS (Ness et al. 2013b) surveys is also typical for b/p bulges originating from disk instabilities (Gonzalez & Gadotti 2016). Babusiaux et al. (2010) studied kinematics (radial velocities and proper motions) and metallicities of a sample of bulge stars spread out over different latitudes and concluded that metal-rich stars can be associated with a barred population, while the metal-poor can be associated with a spheroidal component or potentially the inner thick disc. Additionally, Ness et al. (2013b) and Vásquez et al. (2013), who also studied chemo-dynamical properties of bulge stars, arrived at the conclusion that metal-rich stars in their sample belong to the X-shaped bulge, whereas the metal-poor do not. These results and some dynamical simulations (e.g., Di Matteo et al. 2014) allow the existence of a minor spherical component, while most of the mass in the bulge originates from the disk. Shen et al. (2010) modelled the cylindrical rotation in the bulge and concluded that the mass of the spheroidal component can at largest be 8% of the disk mass in order to reproduce the BRAVA observations.

Other observational data that question the classical bulge theory concerns the young stellar population found in the bulge. van Loon et al. (2003) found stars as young as $\lesssim 200$ Myr across the inner bulge. More recent studies of blue stragglers by Clarkson et al. (2011) and microlensed dwarfs by Bensby et al. (2017) have suggested that there is a stellar component in the bulge with ages $\lesssim 5$ Gyr. While the classical bulge theory can explain intermediate-age stars that diffused from the inner disk into the bulge, the presence of a very young stellar population is not expected whatsoever. On the contrary, bulges formed through disk instabilities can, and, in fact, might be expected, to contain young stars (Gonzalez & Gadotti 2016).

The Milky Way bulge is the closest bulge we can observe and the only one we can study in great detail. This advantage is also the reason why the bulge formation scenario and, consequently, the origin of the Galaxy itself are still under debate: the bulge extends

[2] Here we refer to the three major components A, B and C out of five detected in total

over a large area on the sky (more than 150 square degrees according to Figure 3.1) and would require a huge amount of work to be studied homogeneously. Apart from stellar kinematics (if unaltered over time), the evolutionary history of the Galaxy is imprinted in chemical abundances as well, making spectroscopic examination of the bulge stars particularly important. Trends of stellar abundance ratios with metallicity can, through Galactic Chemical Evolution models (GCE; e.g., Matteucci 2012), shed some light on the initial mass function (IMF, describes the distribution of stars according to their mass at birth), star formation rate (SFR) and gas inflow time-scales in different parts of the Galaxy. Ideally, information about chemical abundances should be combined with stellar kinematics to arrive at the full picture.

McWilliam (2016) discusses that, in the case of the secular evolution of the disk, stars both from the thin and thick disk should be present in the bulge. Thus, the metal-rich sub-population of bulge stars, which is concentrated near the Galactic mid-plane and shows a large amount of SNe Ia nucleosynthesis products in their [α/Fe] ratios, is similar to stars from the local thin disk. These bulge stars appear, however, at a higher mean metallicity than the typical metallicity in the thin disk. The metal-poor bulge sub-population, on the other hand, shares similarities with the local thick disk, being spread out at a larger scale height and suggesting a similar or slightly higher SFR rate, but, again, at higher mean [Fe/H] values than in the thick disk.

To quantify the SFR and IMF in the bulge [α/Fe] vs. [Fe/H] trends have been used extensively. An IMF skewed to produce more high-mass stars would move [α/Fe] ratios upwards due to a larger amount of product made in SNe II, which is the main production channel of α-elements, whereas iron is mostly produced in SNe Ia (McWilliam 1997). The [α/Fe]-"knee" is the location where the [α/Fe]-ratio starts to decrease due to the contributions from the yields synthesised in SNe Ia which are delayed by $\sim$1 Gyr. A high SFR would result in the "knee" appearing at higher metallicities. Bensby et al. (2017) compare their α-trends of dwarf stars in the thick disk and bulge and find that there is no significant variation in IMF, but the [α/Fe] "knee", however, appears at slightly higher metallicities than in the local thick disk. They note that this question should be further investigated by analysing larger stellar samples. Jönsson et al. (2017a,b) worked on disk and bulge giants and determined their α-abundances, which led them to a conclusion that the bulge generally follows the thick disk trend, again indicating similar chemical evolution histories. Their results could probably indicate a slightly higher SFR rate in the bulge, too, since the bulge trends of Mg, Ca and Ti trace the upper envelope of the thick disk trends. Johnson et al. (2014) examined α and iron-peak abundances in bulge giants and arrived at a different result: while no special IMF is required to reproduce the bulge trends, they conclude that the bulge and the thick disk have experienced different chemical enrichment paths. This conclusion was drawn from the enhanced abundance trends, in particular of the iron-peak elements such as Co, Ni and Cu, in the bulge compared to the thick disk. In the analysis, however, their reference sample consisted of disk dwarfs, and this sort of

comparison using dwarfs and giants is likely to be affected by potential systematic offsets as discussed below in Section 6.2.1 and also in Meléndez et al. (2008).

Evidently, the literature studies have not arrived at a common solution as some are finding similarities and others find differences between the evolutionary paths of the disk and bulge. As for the extensively studied α-elements, iron-peak elements are also useful in Galactic archaeology, being able to probe the chemical enrichment history. They are produced both in thermonuclear and core collapse supernovae, and therefore can put constraints on the evolution of the local disk and bulge. In this work, we extend the study in Jönsson et al. (2017a,b) and examine six iron-peak elements (Sc, V, Cr, Mn, Co and Ni) conducting a giant-giant comparison of the local disk and the bulge. To provide as homogeneous analysis as possible, all of our spectra are of similar type of stars and restricted to an identical wavelength region, so that the abundances are retrieved from the same atomic lines using the same atomic data. For this purpose, we use high-resolution optical spectra of K giants mainly obtained by the FIES spectrograph at the Nordic Optical Telescope for 291 disk stars and the UVES/FLAMES spectrograph at the ESO Very Large Telescope for 46 bulge stars. The formation of the Galaxy and the bulge are still not fully understood, and today no successful fully self-consistent models for the bulge in the cosmological framework are available (Barbuy et al. 2018). A homogeneous spectroscopic analysis of the same type of stars in the disk and bulge, examining other elements than the α-elements, can give new insights into the question of whether or not the bulge emerged from the disk.

Chapter 2

Scientific background

To achieve our goals, we will use high-resolution spectra of K giants in the optical region to study the iron-peak elements, which are sensitive to formation routes (e.g., Woosley & Weaver 1995; Clayton 2003; Nomoto et al. 2013; Kobayashi & Nakasato 2011). In this chapter, we will discuss the objects, elements and models needed to determine the abundances.

2.1 K giants

FGK-type stars are extensively used in Galactic archaeology studies since they preserve the initial composition of heavier elements of the gas clouds they were formed from, and hence can reveal the path of the Galactic evolution. Giants are particularly interesting because they are intrinsically very luminous and can be observed with high precision at large distances.

There are, however, some issues that make spectroscopic analysis of giants rather complicated. As a star enters the red-giant branch (RGB), it expands and cools. Lower effective temperatures result in many molecular features in the spectra of giants. This becomes especially important for very metal-rich stars and/or stars with lower effective temperatures. Molecular lines located near an atomic line under investigation can make it impossible to determine the line strength which is needed to determine the abundance. The main reason for this is that the normalised continuum cannot be identified. Since abundances are obtained from the contrast of the line and continuum opacities, a falsely identified continuum leads to errors even for high resolutions. Moreover, densely located molecular lines can create a pseudo-continuum, which, again, if taken as the true continuum, leads to errors in measured abundances. Increasing the resolution does not help since the stellar lines have an intrinsic line width in the stars. Molecular lines can also blend atomic lines of interest

which again affects the precision if the blends are not properly modelled.

Another issue concerns the strength of atomic lines in the spectra of giants. Lower surface gravities, which are typical for giants, enhance the strength of spectral lines due to a lower continuum opacity, H^-_{ff}, caused by a lower electron pressure. Moreover, in the optical region, most of the spectral lines arise due to absorption of photons by neutral element species. At lower effective temperatures in the outer atmospheric layers of K giants, where spectral lines originate, the amount of neutral species increases, and hence, the strength of the spectral lines.

Therefore, it can become quite challenging to find unsaturated and unblended lines for the spectroscopic analysis of giants, especially if the considered wavelength region is rather narrow. Moreover, special attention has to be given to departures from LTE due to lower pressures in the atmospheres (more discussion on the LTE and NLTE assumptions can be found in Section 2.3.1 and 2.3.2).

However, these difficulties in the analysis of giants can be overcome if analysed in a careful way, and it has been shown by Jönsson et al. (2017a) that K giants can be as good probes of abundances as dwarfs can. This conclusion was drawn by measuring abundances of α-elements in the Solar neighbourhood giants and benchmarking the results to carefully determined abundances of Solar neighbourhood F and G dwarfs (Bensby et al. 2014). This has an important implication for spectroscopic examination of the Galactic bulge due to the higher luminosity of giants: observations of giants can provide stellar spectra of higher quality without extremely long integration times. This opens up an alternative method to the observations of dwarf stars in the bulge, for which high-quality spectra can only be acquired with modern instrumentation during random microlensing events which enhance the intrinsic luminosity of dwarfs. In the case of giants, however, targets and their positions can be specifically chosen giving a possibility to collect more homogeneous data.

As an example, assume an observed giant and dwarf star with the same apparent magnitude. If the giant star is an Arcturus-like K giant with an absolute magnitude of $M_V^G \approx 0$ (Ducati 2002) and the dwarf star is solar-like with $M_V^D \approx +5$, using the distance modulus we can calculate how the distances between the observed stars relate:

$$m_V - M_V = 5 \log_{10} \left(\frac{d}{10} \right)$$

Inserting the absolute magnitude values from above:

$$M_V^D - M_V^G = 5 \log_{10} \left(\frac{d_G}{d_D} \right)$$

$$\Rightarrow \frac{d_G}{d_D} = 10$$

Hence, an Arcturus-like K giant with the same apparent magnitude as a Sun-like dwarf will be ten times as distant, which is very beneficial when studying the bulge that lies at a distance of about 8 kpc (e.g., Gillessen et al. 2009).

2.2 Iron-peak elements

Nuclear fusion in the core of massive stars ($M \gtrsim 8\ M_\odot$) occurs up to iron since iron is the most tightly bound atom, and fusion of atoms heavier than iron does not produce energy but consumes it. Production of elements heavier than iron, but also of those that are situated in the vicinity of it in the periodic table, occurs during later life stages of stars. For massive stars, such elements are created during core-collapse supernovae, or SNe II. For mass-accreting carbon-oxygen white dwarfs in stellar binaries, these elements can be produced in thermonuclear explosions in SNe Ia, if the total mass of the white dwarf exceeds the Chandrasekhar mass[1].

Iron-peak elements are elements with atomic numbers $21 \leq Z \leq 28$[2], i.e., Sc, V, Cr, Mn, Fe, Co and Ni. In Figure 2.1 the relative chemical abundances in the Solar System are shown. It is evident that there is a peak in abundances around iron, hence, the name "iron-peak". But these elements do not necessarily share the same nucleosynthetic origin.

As it was discussed in Chapter 1, α-elements have been studied in great detail, unlike the iron-peak elements, although, they are also important probes of the Galactic evolution. Originally, it has been thought that iron-peak elements are mainly produced in SNe Ia and to a smaller extent in SNe II, similarly to iron (e.g. Schneider 2015). The true picture is, however, more complicated. Yields of some of these elements appear to be dependent on the metallicity (Woosley & Weaver 1995; Nomoto et al. 2013) and mass (Chieffi & Limongi 2002) of the progenitor star. For this reason, they may also depend on the formation environment and be able to probe evolutionary paths of different stellar populations (e.g. results in Kobayashi et al. 2011).

The proposed nucleosynthetic origins of the iron-peak elements studied are described below.

[1] $M_{Chan} \approx 1.4\ M_\odot$

[2] Note that Ti has $Z = 22$ but is generally considered to be an α-element, i.e., it does not belong to the iron-peak group.

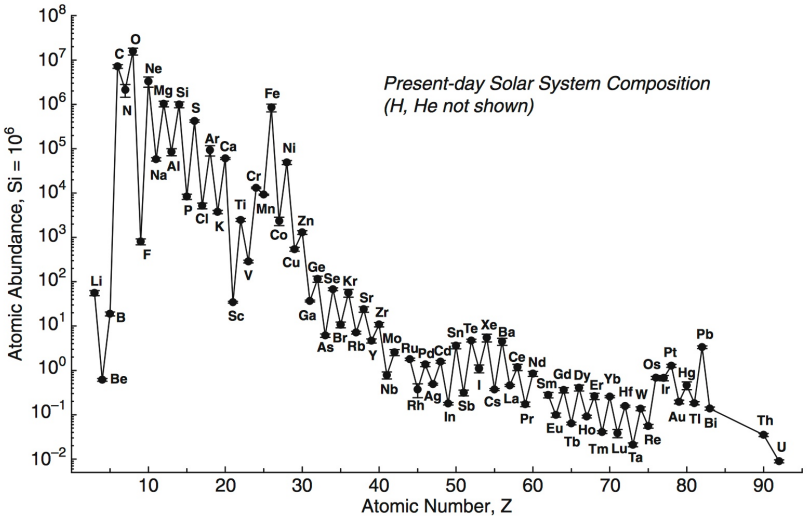

Figure 2.1: The relative Solar System chemical abundances normalised to a silicon abundance value of 10^6 (Lodders 2010).

Scandium

Scandium is the lightest iron-peak element. It has only one stable isotope, ^{45}Sc, and shares some properties similar to those of α-elements (Battistini & Bensby 2015). ^{45}Sc is produced during neon burning and through the radioactive progenitor ^{45}Ti during explosive silicon and oxygen burning (Woosley & Weaver 1995). Most of the ^{45}Sc is thought to originate from SNe II (Clayton 2003) similarly to α-elements. Nevertheless, being the intermediate element between the α-elements and the iron-peak group, the precise origin of scandium is still a subject for debate (e.g. Zhang et al. 2008; Battistini & Bensby 2015).

Vanadium

The only stable isotope of natural vanadium is ^{51}V (99,75% of all V; Clayton 2003), however, the radioactive natural isotope ^{50}V has an extremely long half-life of $1.4 \cdot 10^{17}$ years. ^{50}V is thought to be produced in explosive oxygen and neon burning, while ^{51}V originates from explosive oxygen and silicon burning (Woosley & Weaver 1995). The main cosmic contributor of these isotopes is presumably SNe Ia (Clayton 2003).

Chromium

Natural chromium consists of four isotopes: ^{50}Cr, ^{52}Cr, ^{53}Cr and ^{54}Cr (4.35%, 83.8%, 9.50%, 2.37% of all Cr respectively, Clayton 2003). The two most abundant stable isotopes, ^{52}Cr, and ^{53}Cr, are mainly produced in explosive silicon burning (Woosley & Weaver 1995). ^{50}Cr is predominantly made in explosive oxygen and silicon burning (Woosley & Weaver 1995; Clayton 2003). Yields of the most abundant isotope, ^{52}Cr, produced in

SNe II are much smaller compared to the yields made in SNe Ia. As discussed in Clayton (2003), SNe II occur four-five times more often than SNe Ia, and these two sources produce a comparable amount of ^{52}Cr. Although there are more low-mass than high-mass stars, the rate at which SNe Ia occur also depends on the fraction of binaries, where one of the stars has become a white dwarf and the other star has not yet arrived to the final stage of its life cycle. Moreover, the binary has to be sufficiently tight for the white dwarf to accrete enough matter to reach the Chandrasekhar mass.

The main source of production of the least abundant isotope, ^{54}Cr, is presumed to be SNe Ia (Woosley & Weaver 1995; Clayton 2003).

The atomic line list used here (Gaia-ESO atomic list v.5) does not include the isotopic splitting for the lines used in the analysis. However, the wavelength shift is only 0.003 Å between the lightest and the heaviest Cr isotopes and is, thus, negligible because it will not affect the line width significantly (Heiter et al., in prep.).

Manganese

^{55}Mn, is the only stable isotope of manganese. It is synthesised through radioactive decay of ^{55}Co which is produced in explosive silicon burning and α-rich freeze-out[3]. SNe Ia are probably the main production source of ^{55}Mn (Clayton 2003).

The amount of ^{55}Mn produced in SNe Ia depends, however, on the properties of the progenitor white dwarf. Computations have shown that SNe Ia events occurring at the Chandrasekhar-mass produce more ^{55}Mn than Fe, independent of the metallicity of the white dwarf (e.g., Nomoto et al. 1997; Yamaguchi et al. 2015). Interestingly, SNe Ia events taking place below the Chandrasekhar-mass underproduce ^{55}Mn instead, but the amount of ^{55}Mn yields increases with metallicity (e.g., Woosley & Kasen 2011).

Early nucleosynthesis models indicated metallicity dependent ^{55}Mn yields produced in SNe II (e.g., Woosley & Weaver 1995), but more recent ones produce underabundant ^{55}Mn yields at all metallicities (Kobayashi et al. 2006).

Iron

The three most abundant stable isotopes of iron are ^{54}Fe, ^{56}Fe and ^{57}Fe which correspond to 5.8%, 91.72% and 2.2% of all iron respectively (Clayton 2003). ^{54}Fe is largely produced

[3] α-rich freeze-out occurs in SNe II as a shock wave created in the core collapse propagates through the Si-rich stellar shell. As a result, the nuclei are broken down into nucleons and α-particles because of the high temperature. As the temperature drops, they reassemble producing new heavy nuclei (Jordan et al. 2003).

in explosive silicon burning in SNe Ia (Woosley & Weaver 1995; Clayton 2003). ^{56}Fe and ^{57}Fe are products of the radioactive decay of ^{56}Ni and ^{57}Ni respectively. ^{56}Ni and ^{57}Ni are synthesised in explosive silicon burning and in the α-rich freeze-out. A larger fraction of these unstable Ni-nuclei is produced per each SNe Ia, but a comparable total fraction is produced in the more frequent SNe II (Clayton 2003).

Cobalt

Cobalt has one stable isotope, ^{59}Co, that is mainly created through explosive silicon burning, the α-rich freeze-out and by the s-process occurring in asymptotic giant branch (AGB) stars. It is produced by both SN Ia and SN II mechanisms, but probably more by SNe Ia. Therefore, although Co and Fe have increased in their proportion to H, the [Co/Fe] ratio has been roughly constant throughout the history of the Galactic evolution, apart from the very early times when this ratio was much higher than the solar Co-abundance (Clayton 2003).

Nickel

The two most abundant stable isotopes of nickel are ^{58}Ni (68.3%) and ^{60}Ni (26.1%). These isotopes are largely created both in explosive silicon burning and during the α-rich freeze-out. A substantial amount of ^{60}Ni is also created by the s-process. A larger fraction of ^{58}Ni and ^{60}Ni is produced in SNe Ia, but since SNe II are about four-five times more frequent, the total contribution from these two processes is roughly equal (Clayton 2003).

Similarly to chromium the isotopic shifts were not accounted for in the analysis since the wavelength differences between the dominating Ni isotopes are only $\lesssim 0.03$ Å (Heiter et al., in prep.).

To retrieve the abundances of these elements, we need to synthesise the spectrum of a specific star. To do so, we need to describe the physical state of its atmosphere.

2.3 Model assumptions

In this section, we describe what assumptions are usually made in model atmospheres and spectral line synthesis in order to retrieve the chemical composition from a stellar spectrum. Abundances can also be estimated by measuring the equivalent width of a spectral line, but this method is not suitable in our case for several reasons. First, atomic lines of interest are likely to be contaminated by molecular features in the spectra of K giants, and such blends have to be modelled (see Section 2.1). Additionally, Sc, V, Mn and Co are elements with odd atomic numbers suffering from the hyperfine splitting of atomic levels. This cannot

be accounted for by the equivalent width measurements (see Section 4.1). Therefore, a spectral line synthesiser is preferred instead.

2.3.1 Model atmosphere assumptions

Model atmospheres are essential in spectroscopic analysis and describe the physical state of the gas/plasma of the stellar atmospheres. Most importantly, they reflect how the pressure and temperature depend on optical depth in a stellar photosphere, i.e., in the outer atmospheric layers of the star in question. In practice, a model atmosphere contains tables as a function of optical depth of the fundamental atmospheric parameters, which are the effective temperature (T_{eff}), surface gravity ($\log g$), metallicity ([Fe/H]) and microturbulence, (ξ_{mic}). T_{eff} relates to the total luminosity of a star, $\log g$ determines the gas pressure in the stellar atmosphere and [Fe/H] can be associated with the element mixture, which also determines how much radiation is emitted in the UV or IR from the atmosphere. Metals are efficient absorbers of the UV radiation, and a metal-rich star appears redder since it emits more IR radiation than a metal-poor star. ξ_{mic} is a special line-fitting parameter which describes small-scale, depth-independent motions along the line of sight (Rutten 2003).

To construct a model atmosphere, simplifying assumptions are always made to avoid excessive complexity and prohibitively long computational time.

Hydrostatic equilibrium
This assumption means that the gas in the photosphere does not accelerate, that is, its velocity is zero or constant. This implies that contributions from the pressure and gravitational forces are of equal magnitude. It also means that no dynamically significant mass loss occurs.

Plane parallel or spherical geometry
In a plane parallel atmosphere all physical variables depend on one space coordinate, the geometrical depth. This assumption holds rather well for dwarf stars where the size of the photosphere is much smaller compared to the stellar radius. For giant stars, a more complex spherically symmetric geometry is suitable due to the more extended photosphere. Here, the dependence of the physical variables is multi-dimensional.

Homogeneous or non-homogeneous atmosphere
In the simpler homogeneous case, calculations can be done in one dimension only. A three-dimensional case is more realistic, e.g. it includes convective effects, but it also is more complicated and computationally expensive (Nordlander 2017). E.g., ξ_{mic} is needed in 1-D models which cannot account for small scale motions in stellar atmospheres. In 3-D models

microturbulence is no longer required

Local Thermodynamic Equilibrium
Local Thermodynamic Equilibrium, or LTE, assumes thermodynamic equilibrium at some local temperature in a photosphere. It also implies following:

- the velocity distributions of electrons and ions follow the Maxwellian distribution
- the excitation equilibrium is described by the Boltzmann population distribution
- the ionisation equilibrium is described by the Saha equation
- collisional processes dominate over radiative, i.e., an excited state has a larger probability of collisional than radiative de-excitation

From the criteria above it follows that the source function[4] is described by the Planck function which is purely dependent on the local temperature. In some cases, this might not be valid for different spectral lines, either due to the absorption coefficients that are responsible for the line formation depth or the line source function in the line formation.

2.3.2 Spectral line synthesis assumptions

Usually, when synthesising spectral lines, the same assumptions are made as for the model atmospheres. However, in this context, departures from LTE become more important since they directly affect the features of a spectral line. In brief, the strength of a line can differ from LTE due to a change in line opacity, hence, line formation depth, or departures of the line source function from the Planck function.

In the outer atmospheric layers, the gas density is significantly lower than in the stellar interior, and radiative processes start to be comparable or dominant over collisional processes resulting in an invalidity of the LTE assumption. In this case, the concept of non-LTE, or NLTE, is more suitable. In NLTE one assumes that the velocity of the particles follows the Maxwellian distribution, but the radiative transfer equation is solved properly using the exact source function instead of assuming that it is Planckian. Atomic level populations are then calculated using the equations of statistical equilibrium which account for the influence of the radiation and collisions on the level populations. These calculations are computationally more challenging but, more importantly, they require detailed atomic data which mostly do not exist. This explains why the LTE assumption is still widely used in stellar spectroscopy and might even be better. But the effects of deviations from the LTE should be checked if possible.

[4] The ratio between the emission and absorption coefficients

Spectral lines of all neutral iron-peak elements can be affected by NLTE over-ionisation (a higher amount of ionised atoms than predicted by the Saha equation) and over-excitation (larger numbers of the element that is excited than predicted by the Boltzmann equation). As a consequence, such lines will, in general, be weaker in NLTE compared to LTE (Bergemann & Nordlander 2014) meaning that the measured abundances increase if NLTE is implemented.

Generally, NLTE effects increase with lower surface gravity, lower metallicity and higher effective temperature for atoms that are sensitive to over-ionisation (Bergemann & Nordlander 2014). Lower surface gravity leads to a lower number density of atoms and electrons responsible for collisions in stellar atmospheres. At lower metallicities, the number of scattering electrons decreases together with the line absorption in the UV, leading to over-ionisation which causes larger NLTE effects. Therefore, NLTE abundance corrections increase for the neutral iron-peak elements, such as Cr I, Mn I, Co I and Ni I, with decreasing metallicity. Higher temperatures, on the other hand, strongly increase the radiation field meaning that collisional processes may no longer dominate de-excitation of atoms. (Lind et al. 2012; Bergemann & Nordlander 2014).

Giant stars have lower mass densities than dwarf stars and consequently lower collision rates in their atmospheres. On the other hand, K giants have lower temperatures than dwarfs which decreases the radiation field. For this reason, the question about NLTE effects in giants is non-trivial and requires a detailed investigation.

NLTE effects for iron-peak elements

In the analysis, only lines corresponding to the singly ionised scandium were used. By checking model atmospheres, one can see that Sc II is the majority species in the Sun and K giants in the given temerature range ($\sim$3900 - 4900 K). For this reason, Sc II is not as sensitive to NLTE effects as neutral scandium lines. Zhang et al. (2008) calculated NLTE corrections for their solar Sc II values and the differences were shown to be small (Δ[Sc/Fe] = -0.03 dex). Unfortunately, no information about NLTE corrections for giants was presented.

NLTE corrections for vanadium are still not available, as discussed in Scott et al. (2015); Battistini & Bensby (2015); Jofré et al. (2015). For our K giants, V I is the minority species and might, therefore, be sensitive to NLTE effects. If it is also subjected to over-excitation and over-ionisation like the other neutral iron-peak elements, then NLTE corrections would increase with decreasing metallicity.

Previous studies of metal-poor dwarfs and giants have shown a discrepancy between abundances obtained from Cr I and Cr II lines: singly ionised chromium has a decreasing trend with decreasing metallicity compared to a rather flat trend of singly ionised chromium (e.g., Johnson 2002; Lai et al. 2008). Bergemann & Cescutti (2010) found that this discrepancy disappears when NLTE effects are taken into account. Cr I is the minority species in our K giant stars meaning it is more sensitive to NLTE effects than the majority species, Cr II. Three of our giants, αBoo, βGem and μLeo, overlap with the Gaia benchmark stars in Jofré et al. (2015). The authors calculated NLTE corrections for Cr I: for the metal-poor αBoo ([Fe/H]= -0.57), the NLTE abundance differs by +0.09 dex, whereas for the more metal-rich βGem ([Fe/H] = 0.08) and μLeo ([Fe/H] = 0.20) the corrections are +0.06 and +0.05 dex respectively.

NLTE departures for Mn I have been studied by Bergemann & Gehren (2008). They found that for their sample, mostly consisting of metal-poor dwarf stars, the NLTE corrections range from $\sim$0 dex at solar metallicity, to +0.7 dex at [Fe/H] = -3 dex. However, these results did not account for the hyperfine splitting (hfs) of Mn I lines. Battistini & Bensby (2015) applied their corrections on LTE abundances for a sample of disk dwarfs and found significant differences between the LTE and NLTE abundances, whilst Jofré et al. (2015) who also used the NLTE corrections from Bergemann & Gehren (2008) on their dwarfs and giants, obtained differences that were much smaller. Unfortunately, no NLTE corrections were available for the Mn I line used here.

Bergemann et al. (2010) report NLTE corrections for Co ranging from +0.1 to +0.6 dex for a sample of metal-poor dwarfs ([Fe/H] down to $\sim$ -3) accounting for the hfs. According to the authors, metallicity is the main stellar parameter responsible for the magnitude of NLTE corrections.

Similarly to vanadium, there are no extensive works on NLTE corrections for nickel lines (Jofré et al. 2015). However, Scott et al. (2015) argue that NLTE corrections for Ni I are probably small for the Sun in the optical region. In the case of cooler giants, Ni I is most probably the dominant species having a relatively large ionisation potential, and NLTE effects should be small.

We expect that our results for V I and Cr I are more likely to suffer from NLTE effects since they are the minority species in the examined K giants. The difference in the magnitude of NLTE corrections between the metal-rich and metal-poor stars for Cr I might be $\sim$0.05 dex given the results in Jofré et al. (2015). For V I we are, unfortunately, unable to predict the magnitude of the NLTE corrections.

We have now described the properties of the examined objects and how chemical compo-

sitions can be retrieved from the observed spectra. In the next chapter, we outline more thoroughly the properties of the observed spectra.

Chapter 3

Stellar sample

In this chapter, we provide a description of the properties of the instrumentation and stellar samples originating from the Galactic disk and bulge used in this study. A short summary of these properties can be found in Table 3.1.

The stellar spectra analysed in this comparative study have already been used in previous works by Jönsson et al. (2017a,b), where the stellar parameters (see Section 4.3 for discussion) and chemical abundances of α-elements were determined.

Table 3.1: A summary of the stellar samples.

	Solar neighbourhood	Bulge
Number of stars	291	46
Spectrometer(s)	FIES, ESPaDOnS, Narval	UVES/FLAMES
Telescope(s)	NOT, CFHT, TBL	VLT
Resolution(s)	67000, 65000	47000
S/N	80-120*	16-60
Wavelength region [Å]	5800-6800	

* Not for the spectra from Thygesen et al. (2012), those have $30 \lesssim S/N \lesssim 50$

3.1 Solar neighbourhood sample

In the Solar neighbourhood sample there are 291 K giants. The exact distance to these stars is not known, but they are located inside a sphere with a radius of 1-2 kpc to which the Solar neighbourhood is confined (e.g., Klement 2010). Most of these stars (213) were

observed using the spectrometer FIES installed on the Nordic Optical Telescope (NOT) in May-June 2015 and June 2016, 41 stars were taken from Thygesen et al. (2012) in turn from FIES/NOT spectra, 18 were downloaded from the FIES archives and 19 spectra were taken from the NARVAL[1] and ESPaDOnS[2] spectral archive in the PolarBase data base (Petit et al. 2014). The relation between the number of the thin and thick disk stars in our sample is almost 4 to 1 (see Section 5.1).

The resolution of the FIES spectra is $R \sim$67000 and for PolarBase $R \sim$65000. The entire optical spectrum was covered by these instruments but the wavelength region was restricted to 5800-6800 Å in order to match the wavelength region of the bulge spectra, providing a more homogeneous analysis.

The S/N ratios of the FIES spectra are generally high (for details about the calculation of the S/N ratios see Jönsson et al. 2017a): between 80 and 120; roughly the same applies to the spectra from PolarBase. Spectra from Thygesen et al. (2012) have a lower S/N ratio of about 30-50.

All spectra were reduced and ready to use. No removal of atmospheric telluric lines[3] have been attempted, instead, a telluric spectrum from the Arcturus atlas (Hinkle et al. 2000) was plotted over the observed spectra. For the few cases where stellar lines were affected by telluric absorption, these were avoided.

3.2 Galactic bulge sample

The Galactic bulge sample consists of 46 K giants. The spectra were obtained using the spectrometer FLAMES/UVES installed at VLT. In total, with the aim of attemting to investigate gradients, five fields were investigated: SW (Sagittarius Window), BW (Baade's Window), BL (Blanco field), B3 and B6. They are marked in Figure 3.1, together with the outline of the Galactic bulge (Weiland et al. 1994), the positions of the microlensed dwarfs from Bensby et al. (2017) and fields analysed in Barbuy et al. (2013), Ernandes et al. (2018), Johnson et al. (2014) and Schultheis et al. (2017) (see Section 6.2.2 for discussion). The fields B3, BW, B6 and BL were observed in May-August 2003-2004, whilst the SW was observed in August 2011. Due to the dust extinction it is difficult to observe bulge stars in the optical light range, and for this reason it was only possible to observe stars in the lower part of the bulge. Observations of stars in the immediate centre of

[1] Mounted on Telescope Bernard Lyot (TBL)
[2] Mounted on the Canada–France–Hawaii Telescope (CFHT)
[3] Spectral features that arise due to absorption of photons by molecules in the Earth's atmosphere

the bulge require observations in the IR. However, determination of stellar parameters for such observations is still difficult (e.g. Rich et al. 2012) but progress is being made (Ryde et al. 2016, Schultheis et al. 2016, Rich et al. 2017). In the five regions analysed here, the extinction is less severe compared with the surroundings.

The resolution of the bulge spectra is $R \approx 47000$ and the wavelength coverage is between 5800 Å and 6800 Å, which is the same as for the comparison sample in the Solar neighbourhood. The S/N ratio of the spectra in this sample is significantly lower ranging between 10 and 80.

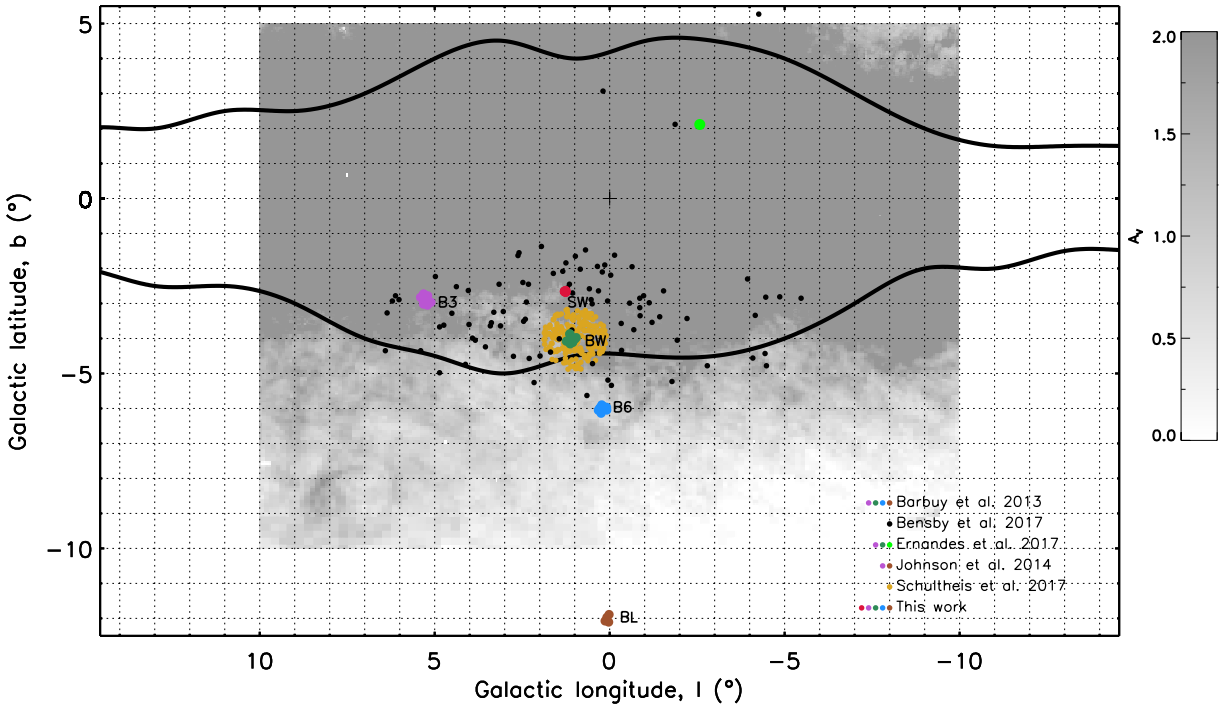

Figure 3.1: The map of the Galactic bulge showing the five analysed fields (SW, B3, BW, B6 and BL). The positions of the microlensed dwarfs from Bensby et al. (2017) and fields analysed in Barbuy et al. (2013), Ernandes et al. (2018), Johnson et al. (2014) and Schultheis et al. (2017) are also marked in the figure. The dust extinction towards the bulge is taken from Gonzalez et al. (2011, 2012) scaled to optical extinction (Cardelli et al. 1989). The COBE/DIRBE contours of the Galactic bulge are taken from Weiland et al. (1994). Credit: H. Jönsson (private communication).

Chapter 4

Methodology

Chemical abundances can be determined from spectra recorded at different spectral resolutions. In general, high spectral resolution, which gets close to completely resolving the stellar lines, yields the most precise and accurate values, but costs more in observing time. E.g., in order to fully resolve a typical thermally broadened ($\Delta v \sim 3$ km/s) iron line, a resolution of $R = c/\Delta v = 100\ 000$ is required. The precision of the abundances is a complex interplay between the type of stars investigated, spectral band, coverage, and S/N ratio (e.g. Rich et al. 2017). Here, we perform a detailed abundance analysis at resolutions of about 50 000-60 000 which is adequate for this type of work.

In this chapter, we first provide a description of the spectral synthesising tool, Spectroscopy Made Easy, used in the chemical abundance analysis. We also discuss the precision of the previously determined stellar parameters for our stars in Section 4.3. In Section 4.4, the information about the atomic line investigation is presented. The methods used for discriminating between the thin and thick disk are discussed in Section 4.5. Finally, the statistical analysis is presented in Section 4.6.

4.1 Spectral line synthesis

Chemical abundances can be measured by estimating the equivalent width of a spectral line, i.e., the area of the line, or by fitting a synthetic spectrum to the observed one. In both cases, one has to know the atmospheric parameters of the star in question and atomic data for the line under investigation.

For elements with odd atomic numbers[1], one has to consider the hyperfine splitting (hfs)

[1]Here: Sc, V, Co and Mn

of atomic energy levels which arises due to nucleon-electron spin interactions. Such interactions will produce several spectral lines instead of one, as would be the case for elements with even atomic numbers. If hfs is ignored, there is a risk that measured abundances are overestimated since absorption lines with hfs components tend to have larger equivalent widths (Prochaska & McWilliam 2000). Therefore, if the investigated line is saturated, taking the hfs into consideration can de-saturate it. To correctly fit hfs components, a spectral line synthesiser is required because other methods, such as those that are solely based on the equivalent width of a line, are unable to discriminate between contributions from different hfs components.

In this work, we have used the spectral synthesiser Spectroscopy Made Easy (SME; Valenti & Piskunov 1996; Piskunov & Valenti 2017) which is a package written in C++ and IDL. SME can simultaneously fit global stellar parameters and/or some atomic parameters of spectral lines (described below) using an observed spectrum to constrain a synthetic model spectrum. This is done by weighted χ^2 minimisation, i.e., the contribution of each pixel is weighted by the observed spectrum, such that points located close to the continuum weigh more than points in the core of a spectral line.

SME has several advantages compared to other spectral synthesisers, such as a convenient graphic interface, χ^2 minimisation for finding the optimal solution for the fitted spectrum and implementation of the MARCS model atmospheres which have shown to be adequate for this type of analysis.

SME requires the following input data to perform the calculations:

1. Global stellar parameters (initial or fixed; fixed in our case): effective temperature (T_{eff}), surface gravity ($\log g$), metallicity ([Fe/H]), radial velocity (v_{rad}), element abundances ([X/Fe]), projected equatorial rotational velocity ($v \sin i$), macro- and microturbulence (ξ_{mac} and ξ_{mic})
2. Atomic/molecular line parameters (initial or fixed; fixed in our case): element name, transition wavelength (λ_T) ionisation state, lower state excitation energy (χ_{exc}) oscillator strength ($\log gf$), damping parameters (radiative, Stark, van der Waals)
3. Wavelength intervals specifying atomic line(s) of interest and continuum points, i.e., line and continuum masks. In our case, they were manually defined and visually inspected in each segment used in the study. Here, a segment is a wavelength region of about 10 Å containing the investigated spectral line and continuum, such that at least three continuum regions are present to ensure a proper continuum adjustment. It is important to carefully select continuum masks such that they fit all of the spectra since adopting individual continuum masks for each star would be too time consuming. The main difficulty is to find continuum positions that remain correct in the spectra of both metal-poor and metal-rich stars since the latter are more affected

by molecular contamination. Line masks, on the other hand, sometimes need to be individually adjusted in the case of atomic, molecular and/or telluric contamination.

4. An observed spectrum. The sampling of it will determine the model sampling.
5. A model atmosphere (see Section 4.2 for details).
6. A set of free parameters to fit that could be one or more stellar parameters, one or more chemical abundances, and/or one or more atomic/molecular parameters ($\log gf$, van der Waals damping). In this study, the free parameter was the chemical abundance of one element. The final chemical abundances were determined using all lines of an element at once.

In addition to stellar and line parameters, SME can also fit some observational properties such as continuum level and spectral resolution.

To scale stellar abundances w.r.t. solar, SME uses solar abundances from Grevesse et al. (2007).

4.2 Implemented model atmospheres

In this project, the determination of element abundances in K giants was performed by interpolating in a grid of spherically symmetric, one-dimensional, hydrostatic, LTE MARCS models (Gustafsson et al. 2008). The spectral synthesis is made under the assumption of LTE, but we later add available abundance corrections for Co. A full non-LTE calculation is beyond the scope of this work.

4.3 Stellar parameters

There are several approaches, both photometric and spectroscopic, to determine the stellar parameters, T_{eff}, $\log g$, [Fe/H] and ξ_{mic}. A common method in spectroscopy is to use iron lines. The effective temperature can be measured by requiring equal abundances of Fe I lines with various excitation energies because different lines of the same elements should result in the same abundance regardless of the excitation potential of atomic levels. The ionisation balance of Fe I and Fe II lines can estimate the surface gravity in a similar manner: abundances originating from different ionisation stages of the same element should be equal. Another method to determine $\log g$ is to consider pressure-sensitive wings of strong lines, e.g., Ca I as in Jönsson et al. (2017a). To determine the microturbulence, a flat trend between abundances of strong and weak Fe I lines and corresponding equivalent widths is usually required. The reason is that there exists a high sensitivity of saturated lines to line broadening associated with small-scale motions, whereas weak lines are not susceptible to

that.

All atmospheric parameters used here were determined in Jönsson et al. (2017a,b). In this case, they were not estimated in the way mentioned above, but instead by simultaneously fitting a synthetic spectrum using SME for unsaturated and unblended Fe I, Fe II and Ca I lines as well as $\log g$ sensitive Ca I wings, while T_{eff}, $\log g$, [Fe/H], [Ca/Fe] and ξ_{mic} were set as free parameters. NLTE corrections for Fe I from Lind et al. (2012) were accounted for when calculating the atmospheric parameters, but these were very small.

The comparison between the derived stellar parameters and the literature values of these overlapping stars with the Gaia benchmark (Heiter et al. 2015; Jofré et al. 2014, 2015) sample (βGem, μLeo, αBoo) showed that they generally agree with each other within the uncertainties. The results are shown in Table 4.1. Moreover, nine of our sample stars have temperatures obtained from angular diameter measurements: eight of nine temperature measurements agree within the uncertainties. For surface gravity, 39 Kepler field stars from our sample had asteroseismically determined surface gravities, from which the measured $\log g$ values deviate with a systematic offset of +0.1 dex and a random uncertainty of 0.12 dex (Jönsson et al. 2017a). We are, therefore, confident that the implemented method works well and that the stellar parameters are precise.

Representative uncertainties in the stellar parameters for a disk star are ±50 K for T_{eff}, ±0.15 dex for $\log g$, ±0.05 dex for [Fe/H] and ±0.1 km/s for ξ_{mic}, but their magnitudes strongly depend on the S/N ratio (see Figure 2 in Jönsson et al. 2017a).

Table 4.1: Stellar parameters of the overlapping Gaia benchmark stars. Top row for each star: the results presented in Heiter et al. (2015); Jofré et al. (2014, 2015); bottom row: the results presented in Jönsson et al. (2017a) and used in this work.

Star	T_{eff} [K]	$\log g$ [dex]	[Fe/H] [dex]	ξ_{mic} [km/s]
βGem	4858 ± 60	2.90±0.08	0.08 ± 0.16	1.28 ± 0.21
HIP37826	4835	2.93	0.07	1.24
μLeo	4474 ± 60	2.51 ± 0.11	0.20 ± 0.15	1.28 ± 0.26
HIP48455	4461	2.65	0.23	1.55
αBoo	4286±35	1.64 ± 0.09	-0.57 ± 0.08	1.58 ± 0.12
HIP69673	4251	1.72	-0.57	1.64

In the HR-diagram in Figure 4.1, the measured $\log g$ and T_{eff} for our disk and bulge stars are plotted and colour-coded with [Fe/H]. The measured values align along the red giant branch and have an expected metallicity spread. This, together with low temperature and

surface gravity deviations from the more precise methods above, imply that the stellar parameters determined are likely to be accurate. This is despite the fact that the stellar spectra, used in the stellar parameter determination, were restricted to a rather narrow wavelength range (5800-6800 Å). Accurate estimations of stellar parameters are crucial for precise abundance measurements since the former are used to create a synthetic spectrum from which abundances are obtained.

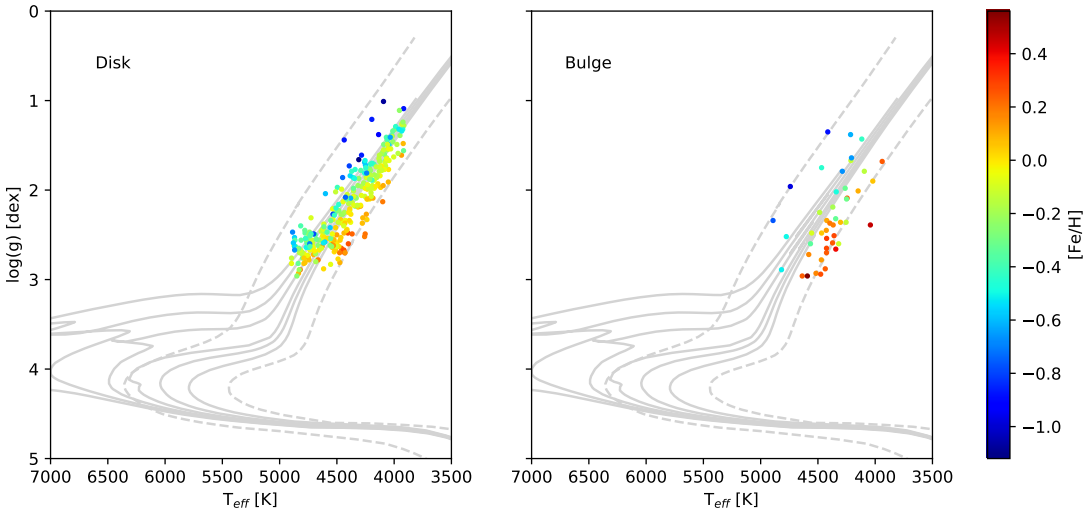

Figure 4.1: HR-diagram showing the disk (left) and bulge (right) giants analysed in this work. The gray solid lines are isochrones for [Fe/H]= 0.0 dex with ages 1-10 Gyr; the dashed gray lines are isochrones for [Fe/H] = -1.0 dex and age 10 Gyr as well as [Fe/H] = +0.5 dex and age 10 Gyr. The isochrones are taken from Marigo et al. (2017).

4.4 Line data

Precise and accurate properties of the atomic transitions corresponding to spectral lines are crucial when estimating abundances from observed spectra. As discussed in Section 4.1, the synthetic spectrum is fitted using the atomic parameters, such as λ_T, χ_{exc}, $\log gf$ and broadening parameters, therefore, retrieved abundances are directly dependent on the quality of the atomic line data.

4.4.1 Atomic data

The line data used in the determination of chemical abundances for all elements apart from Sc were taken from the Gaia-ESO line list version 5 (Heiter et al. 2015, Heiter et al., in prep.). Since the hfs components for Sc were not present in the Gaia-ESO line list, they

were instead taken from the updated version of the VALD line list (Kupka et al. 1999; Pakhomov et al. 2017).

4.4.2 Examined atomic lines

From numerous very careful studies using optical spectra of dwarf stars, as well as careful analysis of the solar spectrum, there is much "general knowledge" about suitable spectral lines to use when analysing dwarf spectra. However, since the number of studies on giant stars is much lower, the same consensus on which spectral lines to use and to avoid is not yet reached. Therefore, all potential atomic lines must be tested and selected according to following criteria:

- Precise atomic data: $\log gf$-values preferably marked as reliable in the atomic line list.
- Unsaturated: equivalent width, W, in the range $5 \lesssim W \lesssim 150$ mÅ. Saturated strong lines are not as sensitive to abundances as weak lines and should, henceforth, be avoided since they can give systematically incorrect results. Very weak lines, on the other hand, can easily be affected by the noise in the spectrum.
- Unblended: one element of interest contributes to absorption at a given wavelength.

All the atomic lines used in the analysis are listed in Table A.1.

4.4.3 Discarded atomic lines

As it was mentioned above, some of the lines investigated were not suitable for the abundance analysis. These lines are listed for completeness in Table 4.2 together with the comments specifying the motivation for the choice.

Table 4.2: Atomic lines that were examined and not used in the final analysis and a comment explaining the reason.

Element	Wavelength [Å]	Comment
Sc I	6210.6	Had precise atomic data but was saturated
Sc II	6279.7	Very strong telluric blend
V I	6081.4	Blend
V I	6119.5	Presumably an imprecise $\log gf$-value
V I	6504.1	Presumably an imprecise $\log gf$-value and/or blend
Cr I	6501.2	An imprecise $\log gf$-value
Cr I	6538.6	Blend
Mn I	6013.4	Had precise atomic data but was saturated
Mn I	6016.6	Had precise atomic data but was saturated
Mn I	6021.8	Had precise atomic data but was saturated
Co I	5915.5	Strong telluric blend
Co I	6429.9	Blend
Co I	6770.9	Had precise atomic data but was saturated
Ni I	5846.9	Blend
Ni I	6128.9	Blend
Ni I	6176.8	Blend
Ni I	6191.1	Blend
Ni I	6327.5	Blend
Ni I	6414.5	Blend
Ni I	6586.3	Blend

4.5 Thin and thick disk separation

As discussed in Chapter 1, the thin and thick disk stellar populations show some substantial differences in [α/Fe] abundances, kinematics and ages. Since we have a sample of disk stars, we would like to separate the thin and thick disk in order to have more homogeneous stellar samples.

Ages of giant stars are rather hard to determine. For dwarf stars, ages can be estimated from isochrones in the HR-diagram, especially at the turn-off, but isochrones on the red

giant branch overlap strongly which makes age determination from this method very difficult, if not impossible. There are other methods to determine the age of giants where their masses are related to the age. For instance, asteroseismology provides information about the stellar interiors and the current masses of giants (e.g. Chaplin & Miglio 2013, Lagarde et al. 2015). Through models, the current mass can be used to estimate the initial mass of a giant (Ness et al. 2016), which is related to the main-sequence lifetime (Martig et al. 2016). Another method to estimate the mass and, hence, the age of giants, is based on measuring abundances of carbon and nitrogen, which are products of the CNO-cycle in stellar cores and are brought up to the surface through convective mixing. The final [C/N] ratio is mass-dependent and can, therefore, be used to estimate the age (Martig et al. 2016). These methods rely, however, on models which can result in systematic errors. In any case, age determination of the giants analysed here is beyond the scope of this work.

If the Galactic space velocities (U, V, W) are known, they can be used to separate the disk components according to stellar kinematics by, e.g., calculating the probability of a star belonging to one of the disk components as presented in Johnson & Soderblom (1987).

Bensby et al. (2014) found, however, that stellar ages of dwarfs act as a better discriminator between the thick and thin disk than the kinematics, although, stellar ages are often subjected to larger uncertainties. They also saw an age-[α/Fe] relation by studying the [Ti/Fe] ratio as it shows a clear enhancement of the thick disk compared to [Fe/H]. They concluded that dwarf and sub-giant stars older than 8 Gyr exhibit higher [Ti/Fe] ratios, and Ti abundances can, therefore, be used to distinguish between the old and young stellar populations, at least in the Solar neighbourhood.

Not all of our stars had measured Galactic velocity components, but instead α-element abundances (O, Mg, Ca and Ti) were available from Jönsson et al. (2017a) for the same stellar sample as here. For this reason, we decided to use titanium abundances since the separation between the disk components was the most clear in the [Ti/Fe] vs. [Fe/H] trend. To improve the separation further, we also included heliocentric radial velocities, v_{rad}, measured from the spectra in Jönsson et al. (2017a).

The separation itself was done using a clustering method called the Gaussian Mixture Model (GMM), which was obtained from the `scikit-learn` module written in Python (Pedregosa et al. 2011) that contains the `GaussianMixture` package. The GMM is a statistical tool which assumes that the overall distribution of the data points consists of (multi-dimensional) Gaussian sub-distributions. The GMM utilises an expectation-maximisation (EM) algorithm, which first calculates the probability of the data points to belong to one of the clusters and then updates the parameters of the Gaussian sub-distributions, i.e., the location and shape of the clusters, using the estimated membership probability. Each iteration of the EM algorithm increases the log-likelihood of the model improving the fit

to the data until it converges. One of the advantages of the GMM is its ability to produce elliptical cluster shapes due to the use of the Gaussian distribution. This is very important in our case since our data are not spherically distributed in the [Ti/Fe]-[Fe/H]-v_{rad} dimensions. However, the number of clusters has to be known in advance since it is one of the input parameters.

To check the validity of the clustering, we applied the separation of the disk stars onto the trends of the α-elements in Jönsson et al. (2017a), as shown in Figure 4.2. The separation seems to be satisfactory, although it is difficult to separate the thin and thick disk stars at the very high metallicity end, where these two components likely overlap each other. The separation shown in Figure 4.2 was then applied to the iron-peak abundance trends.

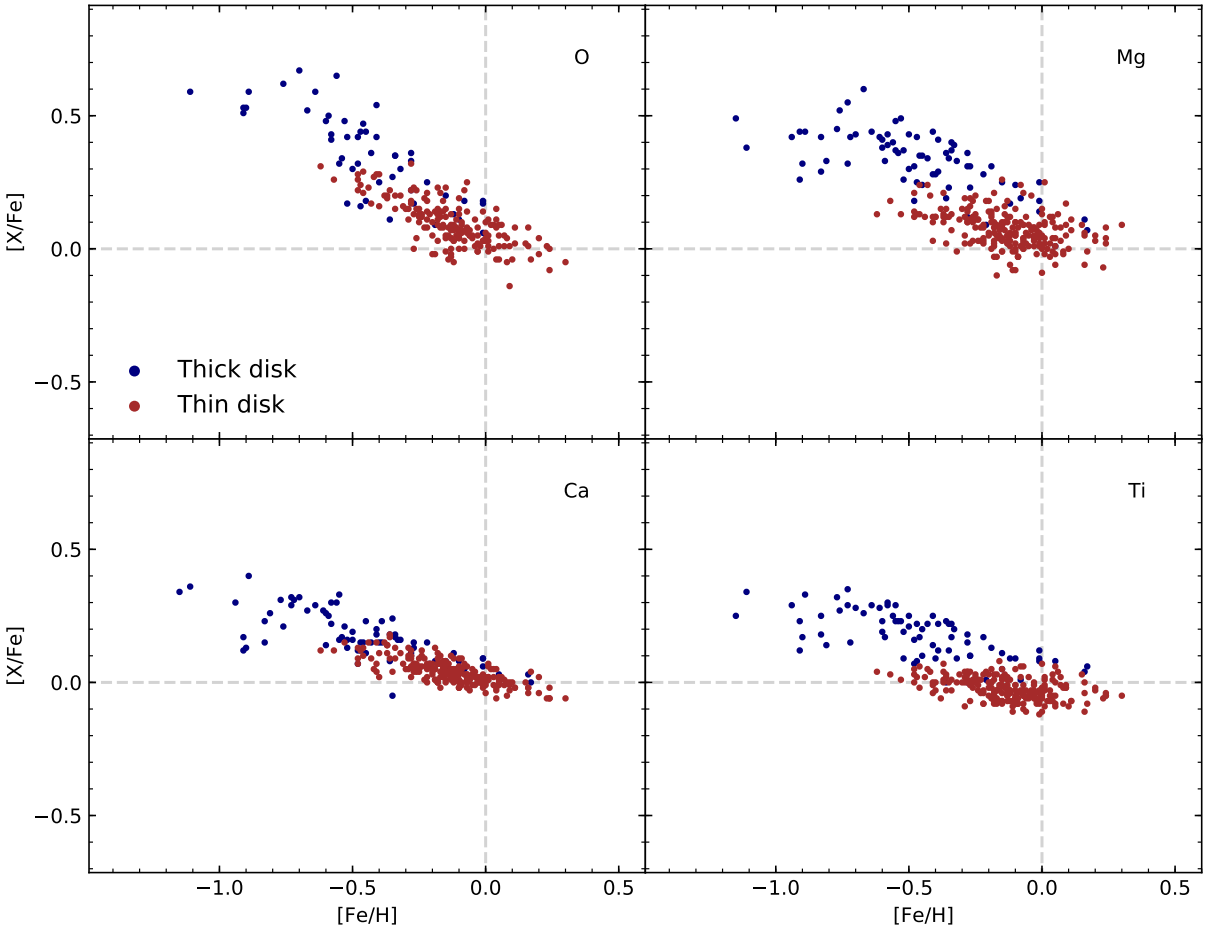

Figure 4.2: The thin and thick disk separation (red and blue dots respectively) applied on the [(O,Mg,Ca,Ti)/Fe] vs. [Fe/H] trends from Jönsson et al. (2017a).

4.6 Abundance uncertainties

Here, we discuss the methodology of the uncertainty estimation, which becomes especially interesting in the context of the results in the next chapter.

4.6.1 Systematic uncertainties

In the analysis of dwarf stars, systematic errors could be eliminated by the normalisation of stellar abundances w.r.t. the Sun. Spectroscopic analysis of giants is more difficult in this sense: the star, w.r.t. which obtained abundances are normalised, should be of the same stellar type, i.e., a giant. Arcturus, or αBoo, is a giant that has been analysed extensively due to its brightness and could be a potential reference candidate. However, despite numerous studies, its stellar parameters and, therefore, abundances are not as nearly precise as the ones of the Sun. Normalising abundances w.r.t. αBoo would then be an additional source of systematic uncertainties. Generally, the origin of systematic errors lies in incorrectly determined stellar parameters, model atmosphere assumptions and atomic data, and are, in general, difficult to estimate. However, in the context of the comparative analysis of the Galactic disk and bulge as carried out here, the systematic errors play a smaller role.

Systematic uncertainties due to the stellar parameters

As discussed in Section 4.3, uncertainties in the stellar parameters will directly affect the measurements of the chemical abundances. To investigate whether the stellar parameters (T_{eff}, $\log g$, ξ_{mic}) have *systematically* influenced the abundance measurements, they were plotted against each other as shown in the panels (a)-(c) in Figure 4.3. Ideally, no trend should be observed in such plots as the stars in our sample were randomly selected and chemical abundances should not be dependent on the effective temperature, surface gravity and microturbulence in the given range.

We fitted a first-degree polynomial to the trends to highlight the slopes. Although small, the [Cr/Fe] ratio increases somewhat with increasing $\log g$ and decreasing ξ_{mic}. We believe that the reason is that one of the Cr I lines used in the analysis is quite strong for certain stars. Strong lines are more sensitive to the surface gravity due to pressure broadening and are strongly affected by the microturbulence due to saturation. Also, a saturated line is not as sensitive to the abundance as a weak line, hence, the [Cr/Fe] ratio is likely to be underestimated at high ξ_{mic}, as shown in plot (c) in Figure 4.3. Although strong lines should be avoided, we decided to use the problematic Cr I line because it largely reduces the overall scatter in the [Cr/Fe] vs. [Fe/H] trend than if only one line was used for Cr I.

The [Mn/Fe] ratio shows a decreasing trend with increasing T_{eff} as well (see plot (a) in Figure 4.3). This could be caused by NLTE effects which increase with temperature. Lines in NLTE tend to be weaker, as discussed in Section 2.3.2, and abundances corrected for NLTE effects are larger. This could potentially eliminate the [Mn/Fe] vs. T_{eff} trend.

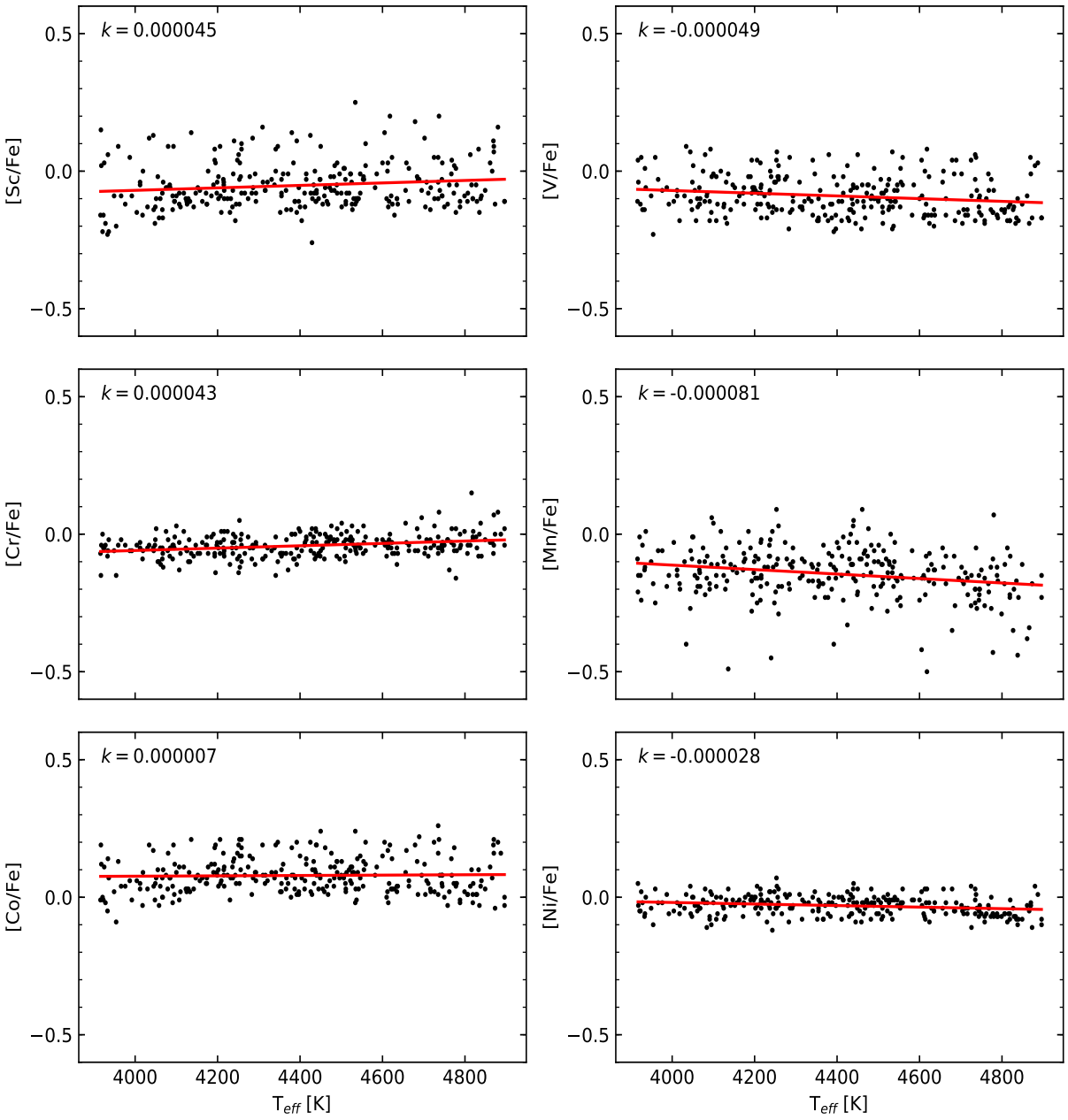

(a) Element abundances as a function of effective temperature.

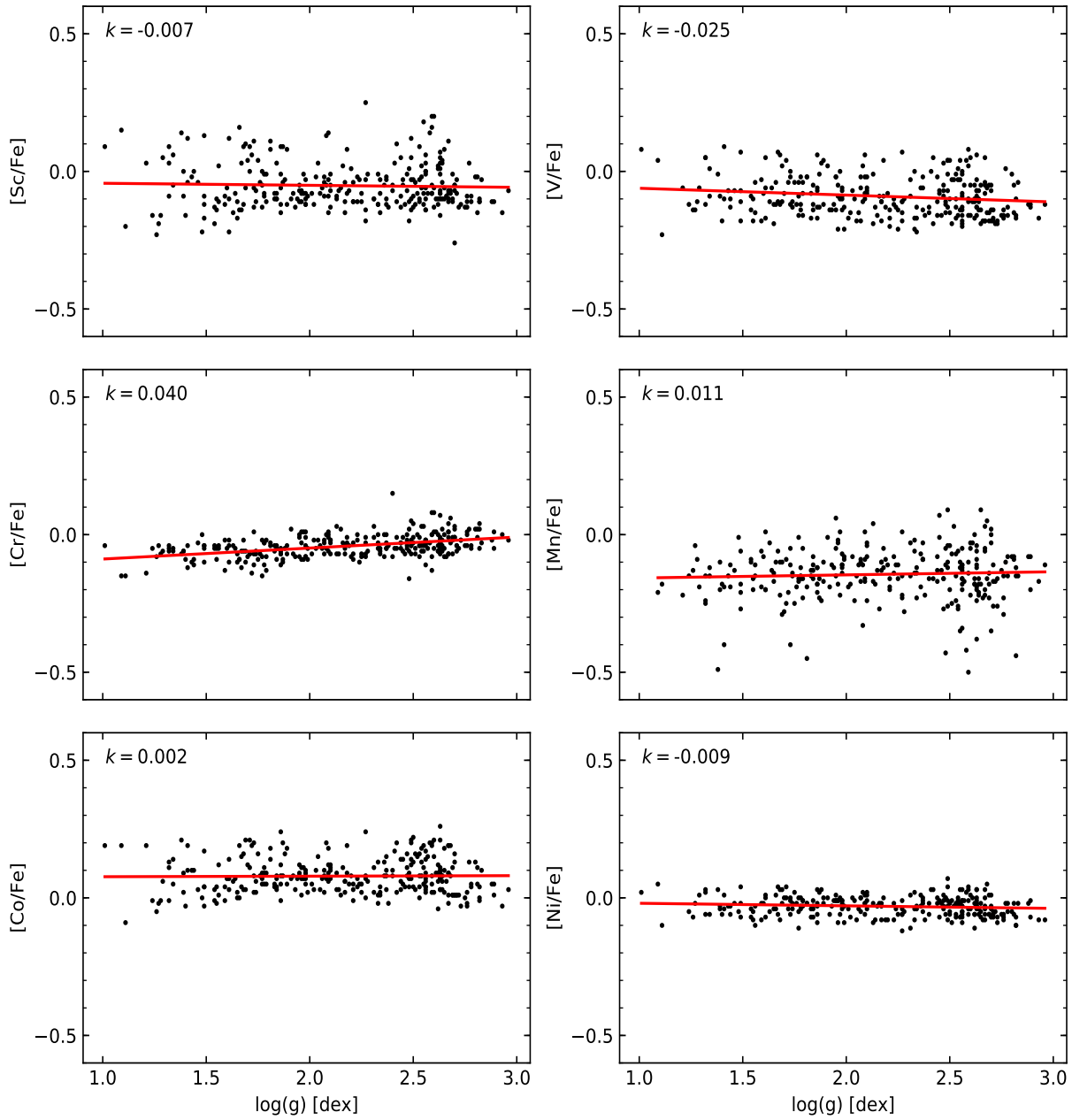

(b) Element abundances as a function of surface gravity.

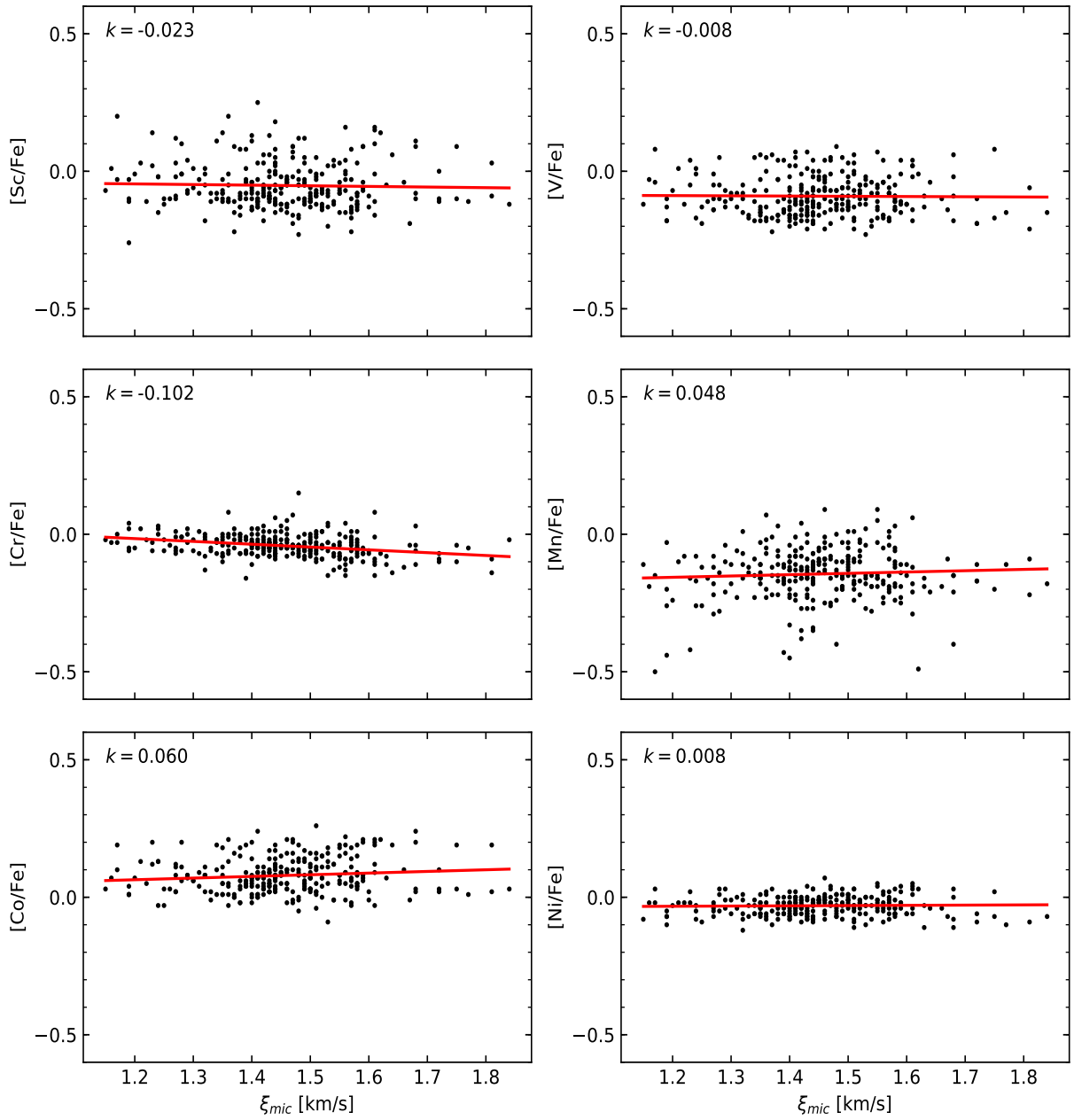

(c) Element abundances as a function of microturbulence.

Figure 4.3: Determined abundances as a function of the stellar parameters T_{eff}, $\log g$ and ξ_{mic}. The solid red line represents the fitted first-degree polynomial with k denoting the slope of the line.

4.6.2 Random uncertainties

Since the uncertainties reported by SME are very small and do not reflect the true uncertainty in determined abundances, we had to use a different method to estimate them. Performing such calculations for every star would be very time consuming; instead, we followed the approach of selecting a typical star in our sample and assigned a typical random uncertainty for each abundance trend. To estimate how *random* uncertainties in the stellar parameters affect the measured abundances, we chose αBoo to be the typical star. Its (FIES) spectrum has a high S/N ratio, allowing us to isolate random errors originating more or less solely from the parameters.

As is often done in the literature, Table 4.3 demonstrates how changes in the stellar parameters influence the abundance measurements. The uncertainties of the stellar parameters come from Jönsson et al. (2017a). From the table we see that Sc is the most sensitive to changes, hence, uncertainties in $\log g$. V and Cr are very temperature sensitive and also have a slightly smaller dependence on variations in the metallicity. Co and Ni, on the other hand, are the most sensitive to the surface gravity and metallicity, while Mn is only slightly dependent on variations in [Fe/H].

Usually, when this type of uncertainty investigation is done, the total uncertainty is deduced as the square root of the sum of $|\delta\mathrm{A(X)}|^2$ accounting for the changes in all stellar parameters as following:

$$\sigma_{param} = \sqrt{|\delta T_{eff}|^2 + |\delta \log g|^2 + |\delta[Fe/H]|^2 + |\delta\xi_{mic}|^2} \tag{4.1}$$

We used Eq. 4.1 to calculate σ_{param} in Table 4.3; for non-symmetrical abundance changes belonging to the same stellar parameter, the mean value of the squared sums was used. Note, however, that these uncertainties are overestimated and can be taken as the maximum possible uncertainty. Stellar parameters determined from a spectrum are correlated, and the exact behaviour of the correlation is difficult to determine. For instance, one can imagine a situation, where an increase in the effective temperature in a K giant would increase the abundance of singly ionised iron, which is sensitive to the surface gravity. Hence, higher effective temperature results in higher surface gravity. But the interplay between all stellar parameters is a complex issue which is difficult to predict, therefore uncertainties are often estimated as if they were uncorrelated.

Table 4.3: Uncertainties in the determined abundances of a typical star (αBoo) due to a change in one of the stellar parameters. The last row represents the combined uncertainty as in Eq. 4.1.

Uncertainty	δA(Sc) [dex]	δA(V) [dex]	δA(Cr) [dex]	δA(Mn) [dex]	δA(Co) [dex]	δA(Ni) [dex]
δT_{eff} = -50 K	-0.01	+0.09	+0.07	+0.02	+0.01	0.00
δT_{eff} = +50 K	+0.01	-0.09	-0.08	-0.02	-0.02	0.00
$\delta \log g$ = -0.15 dex	+0.07	+0.02	+0.02	+0.02	+0.04	+0.05
$\delta \log g$ = +0.15 dex	-0.07	-0.02	-0.02	-0.02	-0.05	-0.05
δ[Fe/H] = -0.05 dex	-0.04	-0.05	-0.05	-0.04	-0.04	-0.04
δ[Fe/H] = +0.05 dex	+0.04	+0.06	+0.06	+0.04	+0.04	+ 0.05
$\delta\xi_{mic}$ = -0.1 km/s	-0.02	-0.01	-0.02	0.00	-0.01	-0.02
$\delta\xi_{mic}$ = +0.1 km/s	+0.02	+0.02	+0.02	0.00	0.00	+ 0.02
σ_{param}	0.08	0.1	0.1	0.05	0.06	0.07

Apart from the approach described above, we tested a more general way for uncertainty estimation - Monte Carlo simulation (MC). For the disk sample, we generated a set of normally distributed random errors with a standard deviation of 50 K for T_{eff}, 0.15 dex for $\log g$, 0.05 dex for [Fe/H] and 0.1 km/s for ξ_{mic}. These uncertainties were then added to the stellar parameters used in the original abundance measurements for αBoo, i.e., all the parameters were changed at once, in contrast to the procedure above. In total, 500 synthetic abundance measurements were carried out. The same procedure was repeated for the bulge sample, again using the stellar parameters of αBoo, but the standard deviations were assumed to be twice as large as compared to the disk.

The standard deviation of the synthetic sample obtained, denoted as σ_{MC} in Table 4.4, shows the uncertainty in the abundances due to random uncertainties in the stellar parameters. Again, the uncertainties were assumed to be uncorrelated producing an overestimated value. Note that the values obtained from MC are similar to the values in Table 4.3. The results of the MC simulation for the disk and bulge are shown in Figure 4.4 and 4.5.

To estimate other sources of errors we also calculated the line-by-line dispersion, σ_{lbl} in Table 4.4, of the abundances for each element apart from Mn, for which only one line was used in the analysis. For the disk sample we again chose the FIES spectrum of αBoo as the representative star, whereas for the bulge, the spectrum of B3-f1 was used as this star has typical stellar parameters and a typical S/N ratio of $\sim$30. The line-by-line scatter represents a combined uncertainty originating from the continuum placement, S/N ratio, uncertainties in $\log gf$-values, unknown line blends and shortcomings of the model atmo-

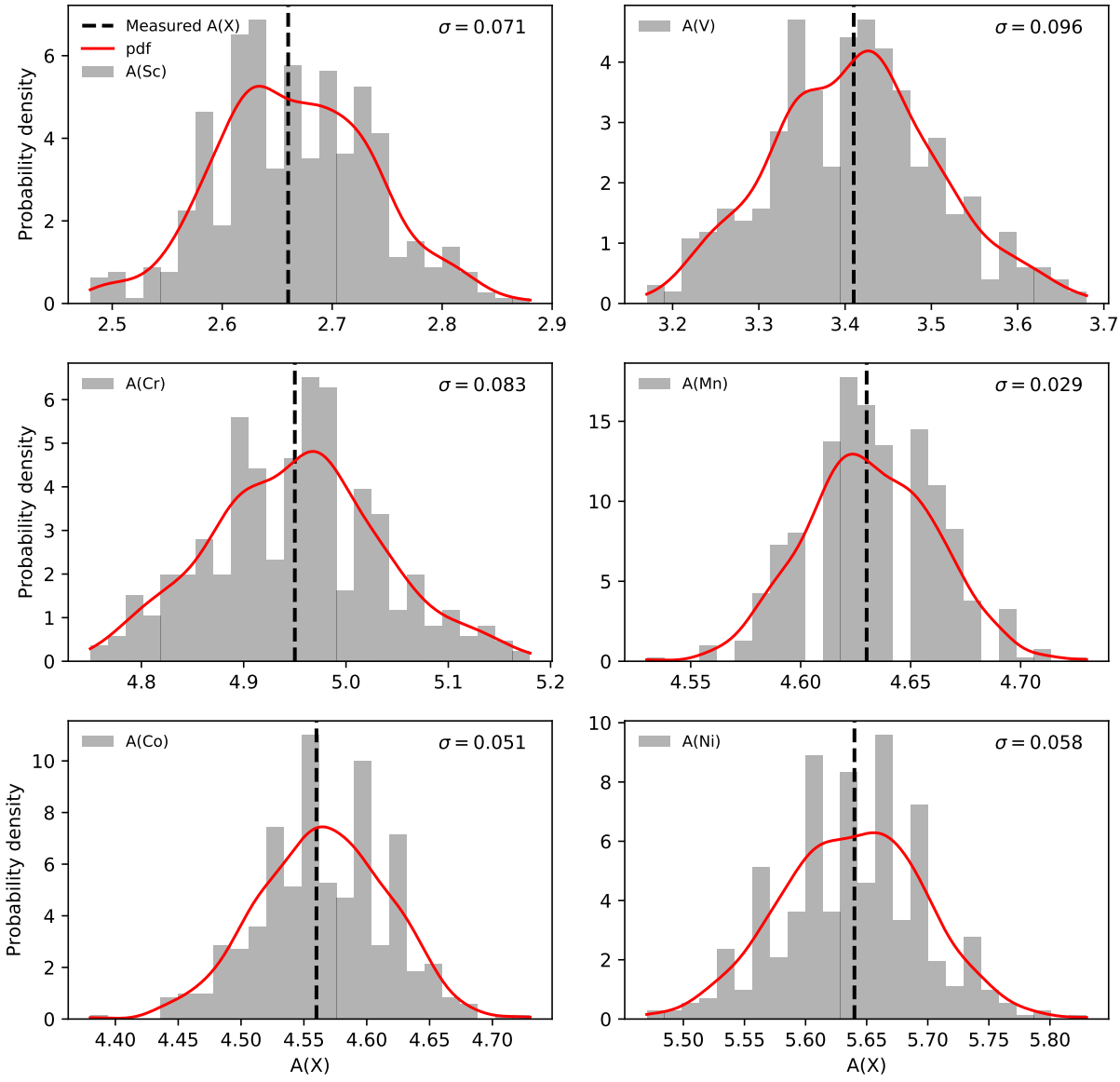

Figure 4.4: Histograms of the abundances determined from 500 synthetic data sets using the spectrum αBoo for the disk sample. The red line denotes the estimated probability density function (pdf) for each element, and σ is the standard deviation of each synthetic sample.

sphere (Johnson et al. 2014). For Mn, the line-by-line dispersion was assumed to be the mean of the values calculated for the other elements. This, of course, does not include the uncertainties originating from the atomic data for the Mn I used. Note that the disk spectra from Thygesen et al. (2012) have much lower S/N ratios and, consequently, larger σ_{lbl} than αBoo. The spectra of αBoo and B3-f1 from which the line-by-line abundance scatter was obtained are presented in Figure 4.6 and 4.7 respectively.

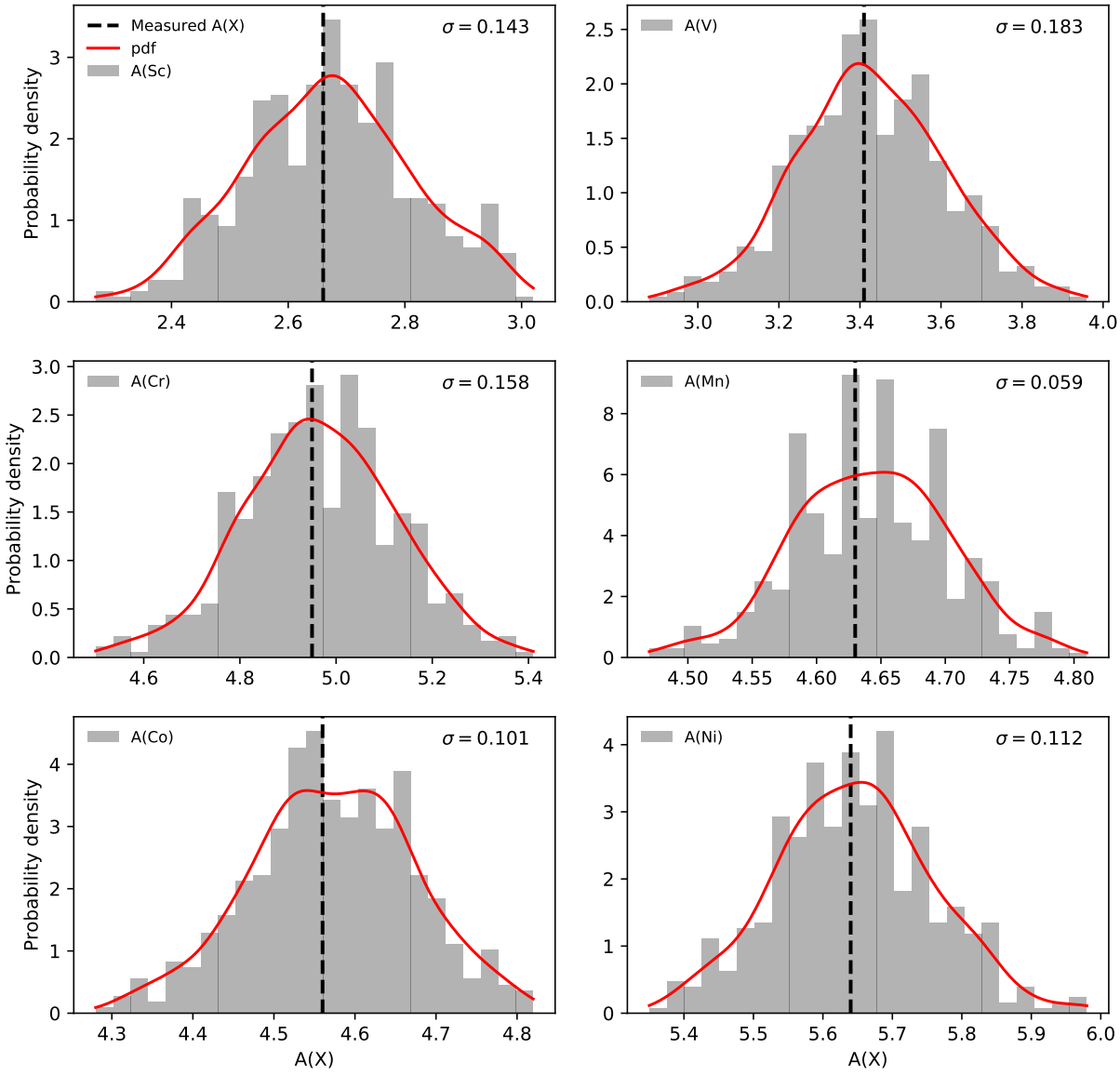

Figure 4.5: Histograms of the abundances determined from 500 synthetic data sets using the spectrum αBoo for the bulge sample. The red line denotes the estimated probability density function (pdf) for each element, and σ is the standard deviation of ech synthetic sample.

The panels (a) and (c) in the first and forth row in Figure 4.6 and 4.7 show a strongly overestimated synthetic spectrum (red) of two V I lines. This divergence is most likely the result of imprecise $\log gf$-values for these lines. In any case, these lines have not been used in the analysis, and they do not affect the fits and measurements done for the lines

of interest, i.e., the adjacent Sc and Co lines.

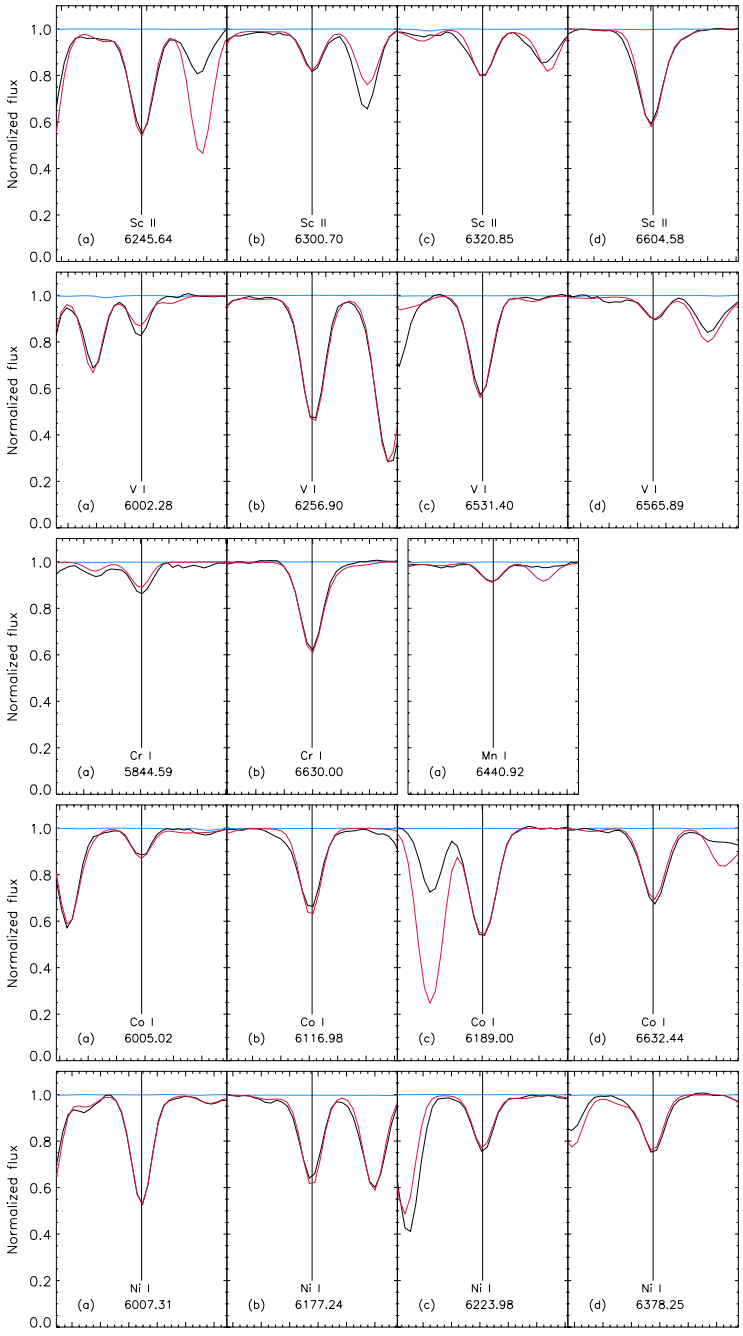

Figure 4.6: Stellar lines used for the calculations of the line-by-line abundance scatter as well as the abundance determination in the analysis in the spectrum of αBoo. The black line is the observed spectrum, the red line is the fitted spectrum and the blue line is the telluric spectrum from the αBoo atlas of Hinkle et al. (2000). The wavelength range of each panel is 1.2 Å, i.e., the large tickmarks correspond to steps of 0.2 Å.

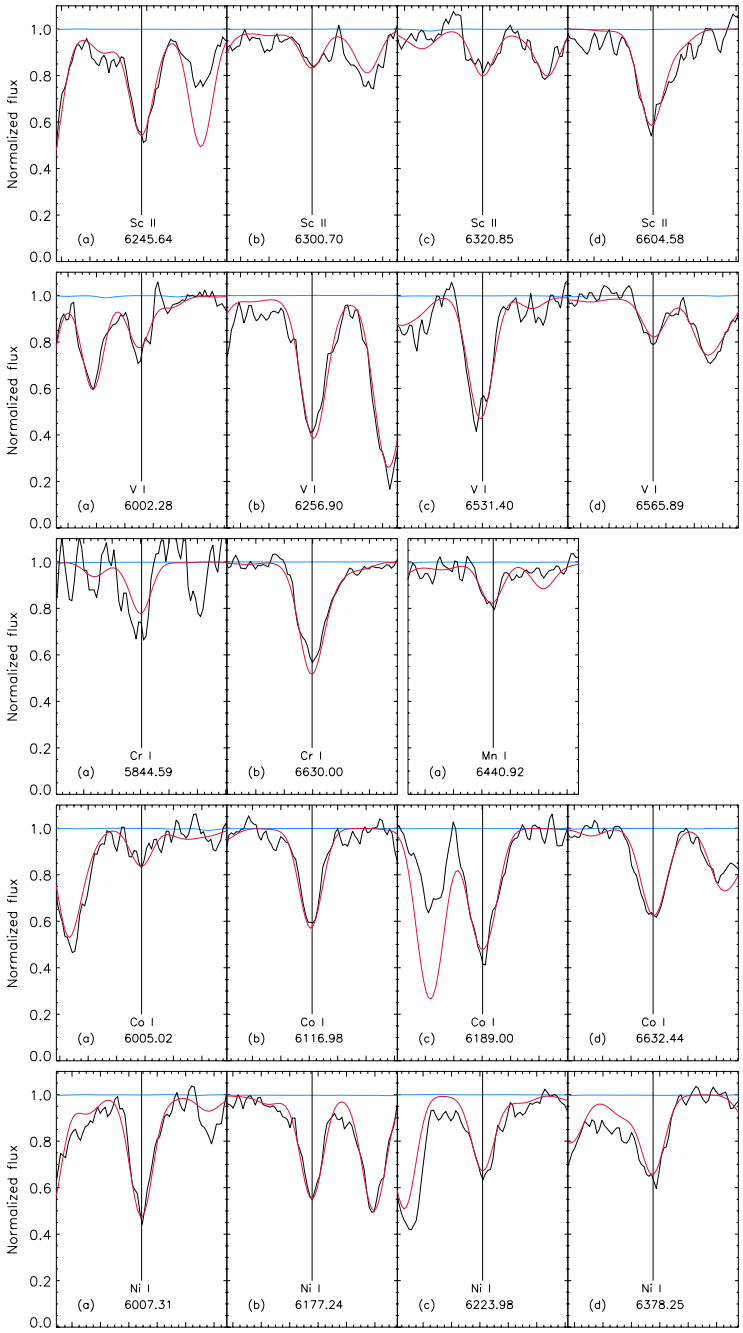

Figure 4.7: Stellar lines used for the calculations of the line-by-line abundance scatter as well as the abundance determination in the analysis in the spectrum of B3-f1. Same colour notations and axes as in Figure 4.6. The Cr I line in panel (a) is strongly affected by the noise and was not used in the final abundance measurement.

The line-by-line scatter is quite large for vanadium and chromium in the disk sample. One

of the two used Cr I lines had a poorly estimated $\log gf$-value which could potentially explain the dispersion. The [V/Fe] vs. [Fe/H] trends of individual V I lines exhibited a significant scatter in general.

The formula for the total uncertainty, σ_{total}, was adapted from Mikolaitis et al. (2017):

$$\sigma_{total} = \sqrt{\sigma_{MC}^2 + \left(\frac{\sigma_{lbl}}{\sqrt{N}}\right)^2} \tag{4.2}$$

where σ_{MC} is the uncertainty obtained by the Monte Carlo method, σ_{lbl} is the line-by-line dispersion and N is the number of lines used in the analysis for each element.

The typical uncertainties obtained in this way are shown in Table 4.4 and were used as the final uncertainty estimations.

Table 4.4: Typical abundance uncertainties for the disk and bulge stellar samples. σ_{MC} represents the uncertainty due to the changes in the stellar parameters using the FIES spectrum of αBoo; σ_{lbl} represents the uncertainty derived from the line-by-line abundance scatter for each element using the FIES spectrum of αBoo (disk) and B3-f1 (bulge); σ_{total} represents the combined uncertainty as in Eq. 4.2.

Uncertainty	Sc	V	Cr	Mn	Co	Ni	Component
σ_{MC} [dex]	0.07	0.1	0.08	0.03	0.05	0.06	Disk
	0.1	0.2	0.1	0.06	0.1	0.1	Bulge
σ_{lbl} [dex]	0.01	0.08	0.09	0.06	0.05	0.05	Disk
	0.04	0.08	0.2	0.1	0.06	0.1	Bulge
σ_{total} [dex]	0.07	0.1	0.1	0.07	0.06	0.06	Disk
	0.2	0.2	0.2	0.1	0.1	0.1	Bulge

In general, the total uncertainties are twice as large for the bulge sample than for the disk, which is expected due to generally lower quality of the spectra. Jönsson et al. (2017b) arrived at a similar conclusion about the uncertainties in the determined α-abundances. For V and Co, the line-by-line scatter is very similar both in the disk and bulge, but for the other elements the scatter is also about two times larger, which is, again, expected.

4.6.3 Comparison with the Gaia benchmark stars

Abundances of the iron-peak elements examined in this work were also measured for the Gaia benchmark stars (Jofré et al. 2015). The comparison between the absolute chemical

abundances is shown in Table 4.5. Our results fall within the uncertainties of the benchmark values for Sc, V and Ni, despite the fact that we used the VALD line list for Sc instead of the Gaia-ESO list.

For Cr and Co our results for μLeo and αBoo fall within the uncertainties of the benchmark values. The results for βGem, on the contrary, do not. Our abundances for βGem deviate the most from the benchmark values in general, and the reason is unclear. βGem is not as metal-rich as μLeo, therefore, any potential atomic or molecular contamination cannot explain the discrepancies. Moreover, the deviations cannot be explained by the quality of the βGem spectrum having a S/N ratio of 90 (cf. $S/N_{\mu Leo} = 89$, $S/N_{\alpha Boo} = 117$). Also, the same atomic lines were used in the analysis for these three stars. βGem is, however, the hottest of the overlapping stars, which could increase NLTE effects due to the higher radiation rate in the atmosphere of βGem. Yet, NLTE corrections applied to our Co abundances (see Section 5.3) were shown to be negligible: $\Delta[\mathrm{Co/Fe}]^{\beta Gem}_{NLTE} \sim 0.0$ dex. If we adapt the benchmark abundance of Cr, βGem will shift slightly lower in the [Cr/Fe] vs. [Fe/H] trend to ([Fe/H], [Cr/Fe]) = (0.07, -0.03) instead of (0.07, 0.04). If the benchmark Co value is adopted, the βGem abundance will appear outside of the Co trend, moving from (0.07, -0.02) to (0.07, -0.1). This means that our abundances more closely follow what one would expect from dwarf trends (see Figure 6.3 and 6.4).

The largest discrepancies are observed for Mn: 0.17, 0.34 and 0.22 dex for βGem, μLeo and αBoo respectively. In the analysis, we only had one satisfactory Mn line which lowers the precision of the measurements. Nevertheless, if these differences are applied to our [Mn/Fe] vs. [Fe/H] trend in Figure 5.1, it would become significantly lower. For example, μLeo, which is located at the outermost metallicity end of the Mn trend and lies at ([Fe/H], [Mn/Fe]) = (0.23, 0.08), would appear outside of the trend as low as at (0.23, -0.26). Furthermore, as seen in Figure 6.3 and 6.4, our trend for Mn is systematically lower at lower metallicities compared to the dwarf sample in Battistini & Bensby (2015). Placing the metal-poor αBoo at (-0.57, -0.44) instead of (-0.57, -0.22) would make this discrepancy even more severe. Therefore, we conclude that the benchmark Mn abundances might suffer from significant systematic uncertainties.

Table 4.5: Iron-peak abundances of the overlapping Gaia benchmark stars. Top row for each star: the abundances presented in Jofré et al. (2015); middle row: our results; bottom row: the difference between our results and the literature values.

Star	A(Sc) [dex]	A(V) [dex]	A(Cr) [dex]	A(Mn) [dex]	A(Co) [dex]	A(Ni) [dex]
βGem	3.28 ±0.12	3.99 ± 0.16	5.66 ±0.04	5.14 ± 0.12	4.90 ± 0.05	6.26 ± 0.05
HIP37826	3.20	3.92	5.73	5.31	4.98	6.24
	-0.08	-0.07	0.07	0.17	0.08	-0.02
μLeo	3.45 ±0.06	4.23 ± 0.06	5.92 ± 0.08	5.39 ± 0.20	5.34 ± 0.09	6.50 ± 0.12
HIP48455	3.40	4.2	5.89	5.73	5.35	6.46
	-0.05	-0.03	-0.03	0.34	0.01	-0.04
αBoo	2.79 ± 0.14	3.49 ± 0.10	5.0 ± 0.07	4.41 ± 0.14	4.48 ± 0.05	5.69 ± 0.08
HIP69673	2.66	3.41	4.95	4.63	4.56	5.64
	-0.13	-0.08	-0.05	0.22	0.08	-0.05

Chapter 5

Results

In this chapter, we present the measured abundances of the examined iron-peak elements. Section 5.1, contains the results of the Solar neighbourhood sample, while the results of the bulge sample are shown in Section 5.2.

Note that our chemical abundances are not normalised relative to the default solar abundances of SME (Grevesse et al. 2007). Instead, absolute solar abundances for all elements apart from Sc were taken from Scott et al. (2015): $A(V)_{\odot} = 3.89$, $A(Cr)_{\odot} = 5.62$, $A(Mn)_{\odot} = 5.42$, $A(Fe)_{\odot} = 7.47$, $A(Co)_{\odot} = 4.93$, $A(Ni)_{\odot} = 6.20$; while the absolute solar Sc abundance was taken from Pehlivan Rhodin et al. (2017): $A(Sc)_{\odot} = 3.04$. The solar values from (Scott et al. 2015) are determined using 3-D model atmospheres and accounting for NLTE effects, which makes them likely to be accurate. However, their solar abundance of Sc is quite large ($A(Sc)_{\odot} = 3.16$) and is much larger than the Sc abundance measured in meteorites in Lodders (2010) ($A(Sc)_{meteor} = 3.07$). Our Sc trend becomes strongly underabundant compared to the dwarf trend in Battistini & Bensby (2015) described in Section 6.2.1 if the solar Sc abundance from Scott et al. (2015) is used. For this reason, we opt for a smaller $A(Sc)_{\odot}$ from Pehlivan Rhodin et al. (2017) which is also more similar to the meteorite Sc abundance.

To highlight the features of the trends, we have also calculated the running mean and running standard deviation which are shown in the plots in Figure 5.1 and 5.2. We let a running window with a constant number of points (29 for the disk sample and 14 for the bulge) move along the metallicity axes in the figures and calculate the mean as well as the 1σ scatter of the trends in each window. The same approach was used later, as shown figures in Chapter 6.

Essentially, the running 1σ scatter should be comparable to the typical uncertainty estimated in Section 4.6.2. Nevertheless, we see from Figure 5.1 that the typical uncertainties

are larger than the scatter for Sc, V, Cr and Ni. The same is observed for basically all of the trends in Figure 5.2. This leads to the conclusion that the random uncertainties were indeed overestimated for these elements.

5.1 Solar neighbourhood

The Solar neighbourhood stellar sample consists of 291 K giants, of which 76 belong to the thick disk and 215 to the thin disk.

The thick disk trend of Sc in Figure 5.1 is enhanced at the low metallicity end reaching [Sc/Fe] ∼+0.25 dex (here and henceforth, we refer to the running mean when describing [X/Fe] ratios). As [Fe/H] increases, the [Sc/Fe] ratio goes down to +0.1 dex. The average ⟨[Sc/Fe]⟩ ratio of the thick disk is +0.17 dex with a mean scatter, ⟨σ⟩, of 0.06 dex. The thin disk trend has the highest [Sc/Fe] ratio of ∼+0.1 dex at [Fe/H]∼-0.4 which decreases and flattens out at [Fe/H] ∼-0.2. This plateau remains even at supersolar metallicities. The average elevation of the ⟨[Sc/Fe]⟩ ratio in the thin disk is +0.03 with ⟨σ⟩ = 0.04.

Vanadium shows an enhancement of ∼+0.15 dex in the thick disk trend at [Fe/H] $\lesssim$ -0.5. The trend gradually decreases with increasing metallicity reaching [V/Fe] ∼+0.1 dex at [Fe/H] ∼-0.1. The mean ⟨[V/Fe]⟩ ratio of the thick disk is +0.13 dex and ⟨σ⟩ = 0.05. The thin disk [V/Fe] ratio is relatively constant and nearly zero apart from a slight increase at supersolar metallicities. The average thin disk ⟨[V/Fe]⟩ ratio is ∼0 dex and ⟨σ⟩ = 0.05.

Chromium abundances in the thick and thin disk show flat trends throughout the whole metallicity range apart from slight enhancements at the highest metallicities in each Galactic component. The mean ⟨[Cr/Fe]⟩ ratio is ∼0 dex with average ⟨σ⟩ ∼0.03 for the thin and thick disks.

The lowest [Mn/Fe] ratio is observed in the thick disk trend with the running mean reaching down to ∼-0.3 dex at [Fe/H] ∼-0.6. The trend steadily increases with increasing metallicity and attains [Mn/Fe] ∼-0.1 dex at [Fe/H] ∼-0.1. The mean ⟨[Mn/Fe]⟩ ratio in the thick disk is ∼-0.2 dex and ⟨σ⟩ = 0.08. The lowest [Mn/Fe] value of the thin disk is ∼-0.2 dex at [Fe/H] ∼-0.4. The trend also increases steadily to [Mn/Fe] ∼-0.02 dex at [Fe/H] ∼+0.1. The average deficiency of the thin disk ⟨[Mn/Fe]⟩ ratio is -0.14 dex with ⟨σ⟩ = 0.06.

The thick disk trend of cobalt gradually decreases from [Co/Fe] ∼+0.2 dex at [Fe/H] ∼-0.7 to [Co/Fe] ∼+0.1 dex at [Fe/H] ∼-0.1. The thin disk trend goes down from [Co/Fe] ∼+0.1 dex at [Fe/H] ∼-0.4 to [Co/Fe] ∼+0.05 dex at [Fe/H] ∼-0.1. At [Fe/H] $\gtrsim$-0.1, the thin disk

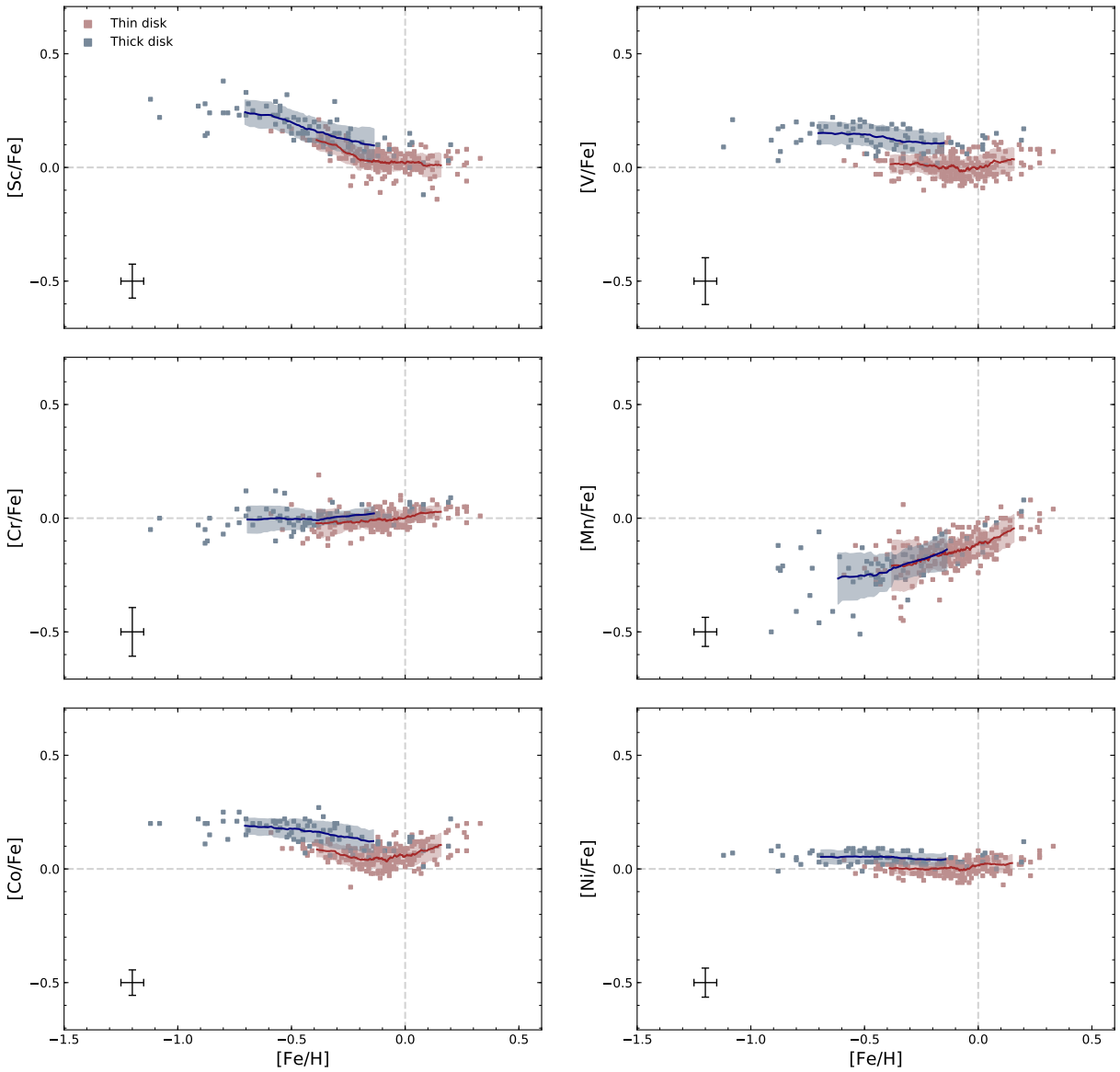

Figure 5.1: [X/Fe] for the examined Solar neighbourhood giants: blue dots denote thick disk stars and pink dots denote thin disk stars. The blue and red solid lines are the calculated running means for the thick and thin disks respectively. The shaded areas are the running 1σ scatter of the thick (blue) and thin (red) disks. The typical uncertainties for each element from Table 4.4 are also shown in the plots.

trend stars to increase up to [Co/Fe] $\sim$+0.1 dex at supersolar metallicities. The average $\langle$[Co/Fe]$\rangle$ for our thick disk trend is +0.16 dex with $\langle\sigma\rangle$ = 0.05 dex and for the thin disk $\langle$[Co/Fe]$\rangle$ = +0.06 dex with $\langle\sigma\rangle$ = 0.04.

The thick disk trend of nickel is rather flat with $\langle$[Ni/Fe]$\rangle$ = 0.05 dex and $\langle\sigma\rangle$ = 0.03. The thin disk trend shows a slight elevation at supersolar metallicites, but the running mean remains relatively flat with $\langle$[Ni/Fe]$\rangle$ about 0 dex and $\langle\sigma\rangle$ = 0.03.

5.2 Galactic bulge

The bulge sample consists of 46 K giants in five different fields: eleven stars in the SW field, ten in B3, nine in BW, eleven in B6 and six in BL.

Jönsson et al. (2017a) concluded that a S/N ratio below 20 has a very strong negative impact on the precision and accuracy of the determined stellar parameters and abundances. For this reason, we only used the abundances obtained from stellar spectra with S/N ratio above 20 (about 30 stars) when calculating the running mean and 1σ scatter. The stars with the S/N ratio below 20 are, however, still plotted in Figure 5.2 but marked differently.

The [Sc/Fe] ratio in the bulge decreases from $\sim$+0.2 dex at [Fe/H] $\sim$-0.5 to $\sim$+0.05 dex at [Fe/H] $\sim$+0.15, where it becomes flat. The average $\langle$[Sc/Fe]$\rangle$ ratio in the bulge is +0.1 dex and $\langle\sigma\rangle$ = 0.10. The vanadium trend in the bulge is relatively flat with $\langle$[V/Fe]$\rangle$ $\sim$+0.19 dex and $\langle\sigma\rangle$ = 0.09. The [Cr/Fe] ratio of $\sim$+0.03 dex at [Fe/H] $\lesssim$ 0 is slightly enhanced compared to [Cr/Fe] $\sim$0 dex at supersolar metallicities. The 1σ spread at [Fe/H] $\lesssim$ 0 is also significantly larger. On average the $\langle$[Cr/Fe]$\rangle$ ratio is 0.02 dex and $\langle\sigma\rangle$ = 0.09. Manganese is steadily increasing in the bulge from [Mn/Fe] $\sim$-0.11 dex at [Fe/H] $\sim$-0.3 to [Mn/Fe] $\sim$0 dex at [Fe/H] $\sim$+0.25. The mean $\langle$[Mn/Fe]$\rangle$ ratio is -0.07 dex and $\langle\sigma\rangle$ = 0.1. The trend of cobalt is rather flat in the bulge with $\langle$[Co/Fe]$\rangle$ = +0.17 dex and $\langle\sigma\rangle$ = 0.07. The [Ni/Fe] ratio does not change significantly with metallicity either, showing $\langle$[Ni/Fe]$\rangle$ = +0.06 dex and $\langle\sigma\rangle$ = 0.04.

We have also plotted the abundances of the iron-peak elements in each bulge field, as shown in Figure 5.3. Given the low number of stars in each field and the large scatter due to the relatively low S/N ratios of the bulge spectra, especially of the stars in the SW field, it is difficult to see any field-dependent trends. More data with higher S/N ratio are needed to investigate how possible trends of iron-peak elements behave in different parts of the bulge.

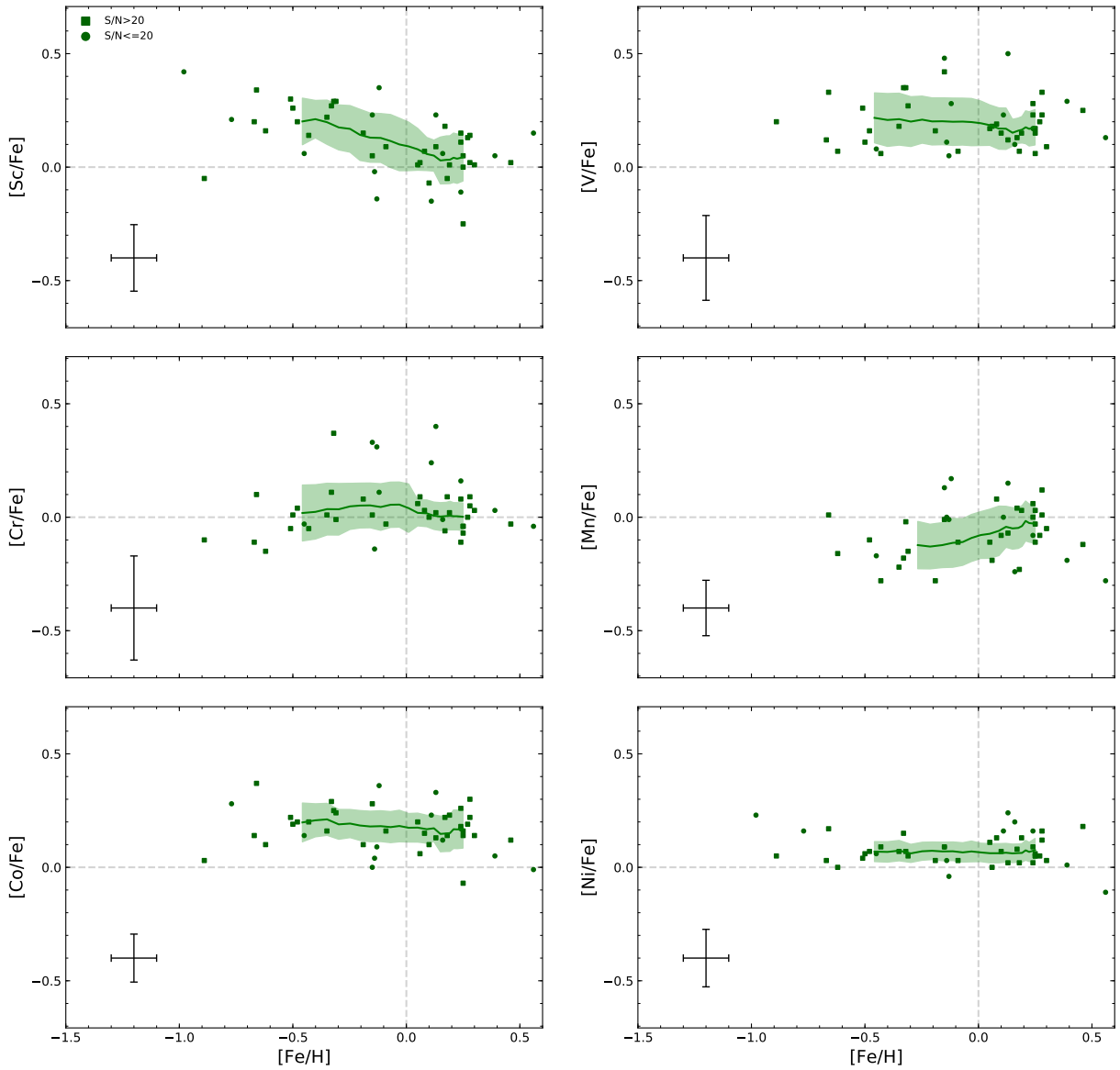

Figure 5.2: [X/Fe] for the examined bulge giants: green squares denote stars with spectra having an S/N ratio above 20, while the green circles denote stars having spectra with S/N ratios ≤ 20. The solid lines represent the running means and shaded areas show the 1σ scatter (only for stars with S/N ratio > 20). The typical uncertainties for each elements from Table 4.4 are also shown in the plots.

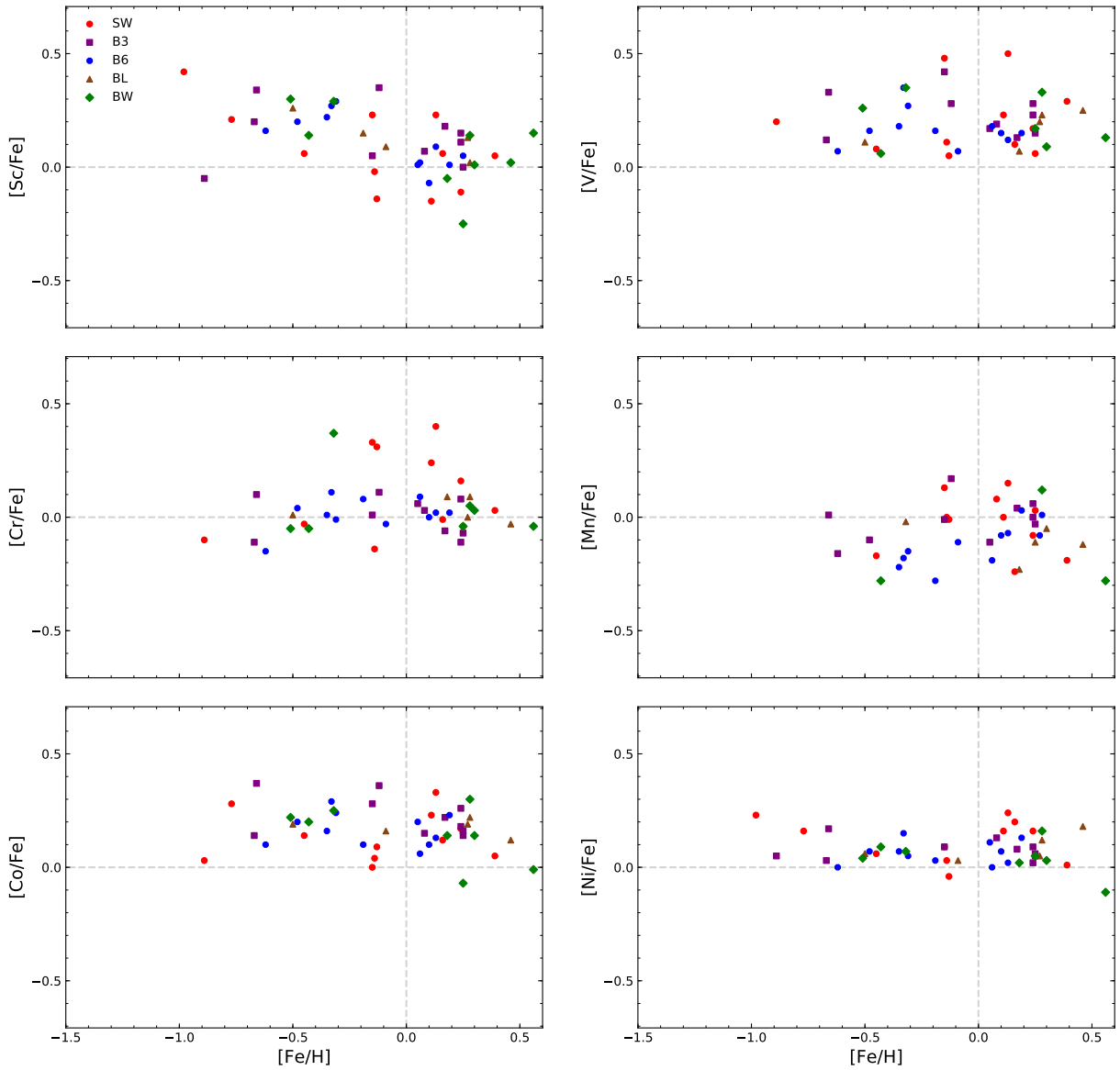

Figure 5.3: [X/Fe] for the bulge giants examined in the bulge fields studied: SW (red circles), B3 (purple squares), B6 (blue octagons), BL (brown triangles) and BW (green diamonds).

5.3 NLTE investigation

Cobalt is the only element for which we were able to calculate NLTE corrections. The corrections were taken from Bergemann et al. (2010)[1].

[1] Available online at `nlte.mpia.de`

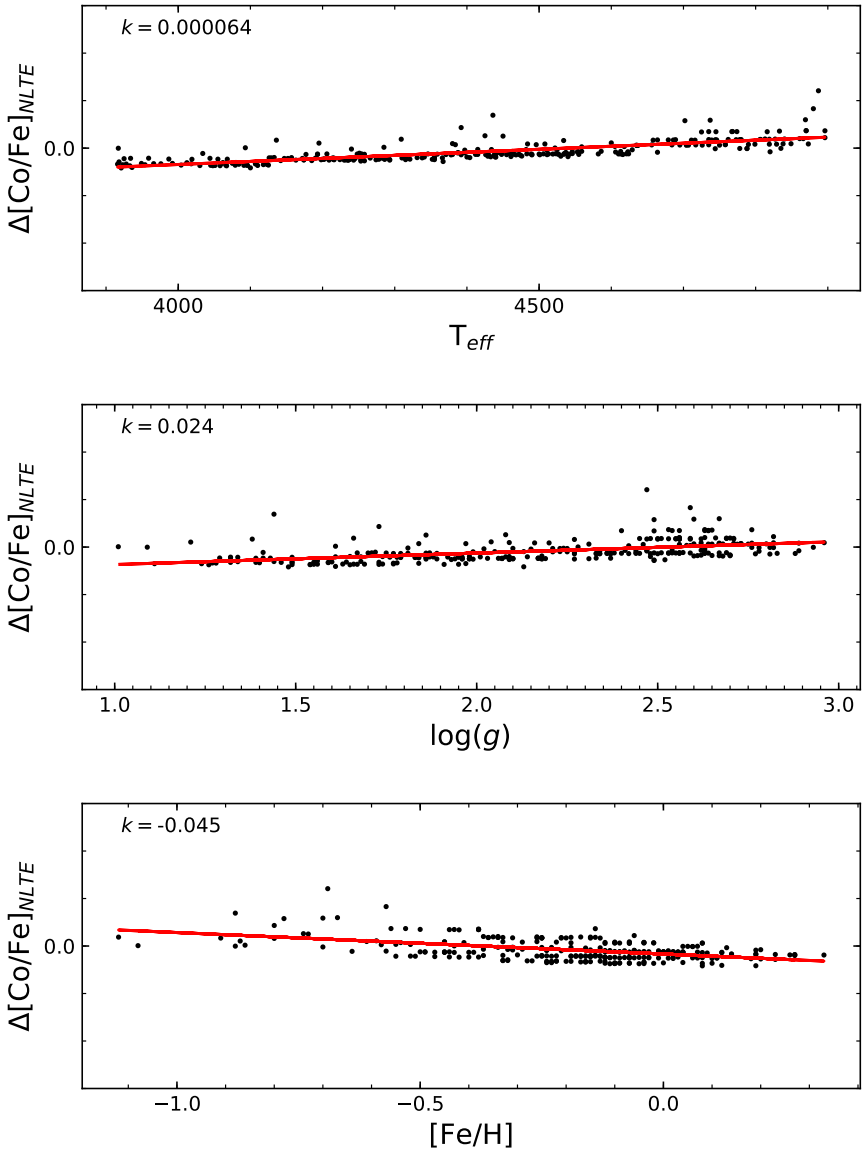

Figure 5.4: NLTE correction for Co in the disk sample (the thin and thick disks combined) as a function of effective temperature (upper panel), surface gravity (middle panel) and metallicity (bottom panel). The red line represents the fitted first-degree polynomial for each trend and k is the slope of the line.

As discussed in Section 2.3.2, metallicity is the main stellar parameter responsible for the magnitude of NLTE corrections, which is visible in Figure 5.4 where we plot the NLTE corrections for all our disk stars against T_{eff}, $\log g$ and [Fe/H]. Again, we fit a first degree polynomial to highlight the slope. The slope of the trend is nearly flat w.r.t. the surface gravity, whereas it slightly increases with increasing surface temperature. For metallicity, the NLTE corrections grow larger with decreasing metallicity as discussed in

Section 2.3.2. In Figure 5.5, we plot NLTE and LTE abundances and running means for these two samples. Overall, the differences are not large, and as a result, the Co trends remain relatively unchanged.

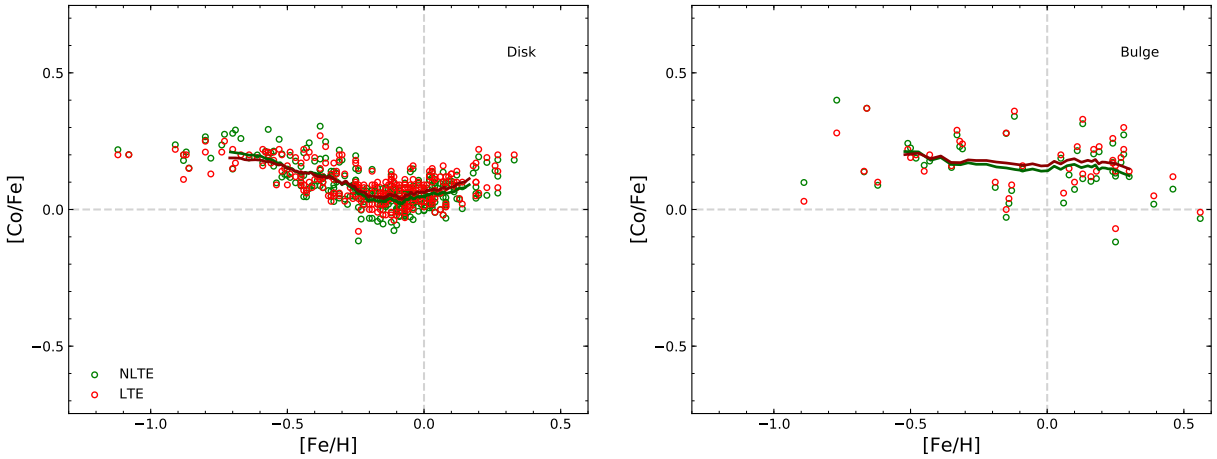

Figure 5.5: Abundances of cobalt calculated assuming LTE (red circles) and using NLTE corrections (green dots) in the disk (left panel; the thin and thick disks combined) and bulge (right panel). The solid lines represent the running means (LTE: red, NLTE: green). Note, that the LTE running mean of the bulge sample was calculated regardless of the S/N ratio, therefore this running mean is different from the one in Figure 5.2.

Chapter 6

Discussion

6.1 Disk and bulge: comparison

To see more clearly how the trends from the local (thin and thick) disk and the bulge relate to each other, we plot them together in Figure 6.1. In this plot we include the running means and running 1σ scatter of the trends in the disk and bulge from Figure 5.1 and 5.2 respectively. We also plot running medians to check the sesitivity of the trends to outliers, as shown in Figure 6.2. The running medians were calculated using a running window of the same size as for the running means (29 data points for the disk and 14 for the bulge). For the bulge, again only the results obtained from the spectra with the S/N ratio above 20 were considered. These trends show similar features, and we only analyse the results for the running means since they produce a smoother curve.

Scandium

Scandium has a complex formation background, being predominantly produced in SNe II, similarly to α-elements (e.g., Battistini & Bensby 2015), and having a dependence on the properties of the progenitor stars such as metallicity (Woosley & Weaver 1995; Nomoto et al. 2013) and mass (Chieffi & Limongi 2002). These relations should make Sc sensitive to the environment in which it is produced.

Our [Sc/Fe] vs. [Fe/H] thick disk trend is more enhanced in [Sc/Fe] than the thin at comparable metallicities , as shown in Figure 6.1. The enhancement of the thick disk in Sc has also been observed in the studies of dwarf stars in Reddy et al. (2006), Adibekyan et al. (2012) and Battistini & Bensby (2015). The bulge trend has an even higher [Sc/Fe] ratio than the thick disk, and at larger [Fe/H], where only the thin disk is present, the bulge trend remains enhanced w.r.t. the thin disk. There is, however, a significant overlap in 1σ

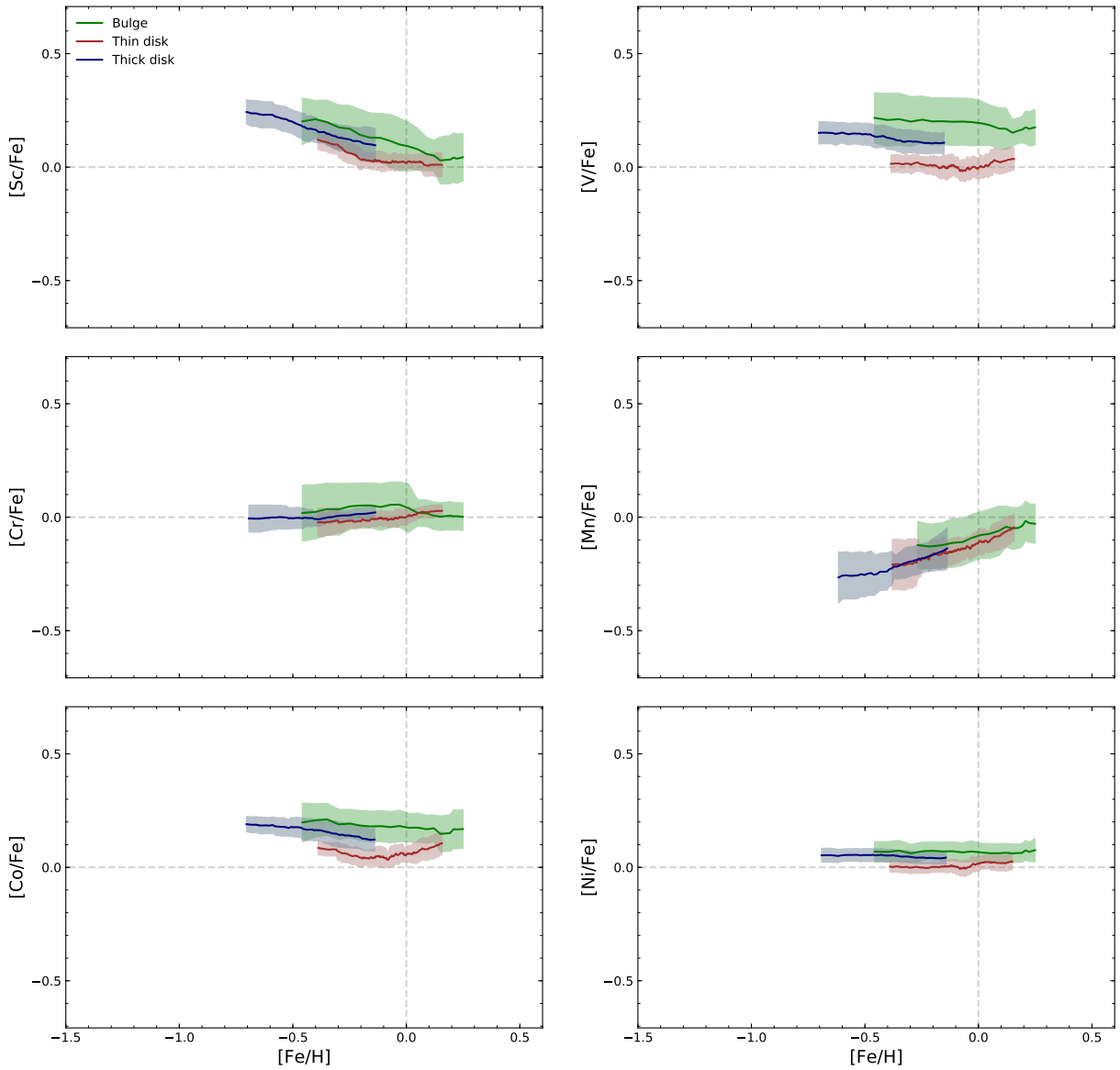

Figure 6.1: The running means and 1σ scatter of the thick disk (blue), thin disk (red) and bulge (green) trends (same as in Figure 5.1 and 5.2).

scatter between all the three trends.

The relation between [Sc/Fe] and [Fe/H] can reflect the SNe II/SNe Ia ratio in a Galactic component. Among the three galactic regions, our thin disk has the lowest [Sc/Fe] ratio, which is consistent with the assumption that the thin disk stars are generally younger (e.g., Bensby et al. 2014), i.e., they formed when the yield contribution from SNe Ia was already significant. Hence, the opposite is valid for the thick disk: many of those stars are old and

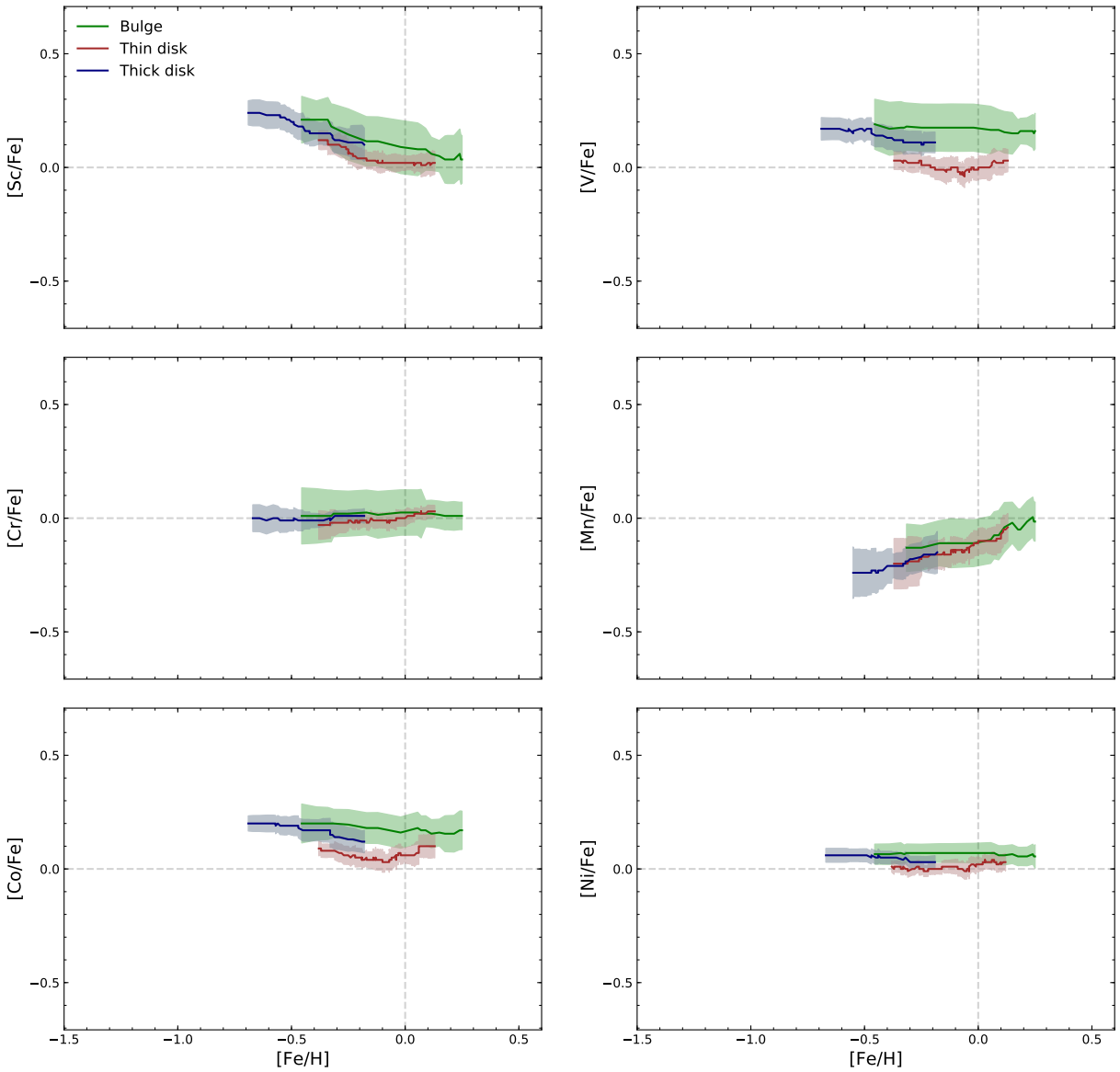

Figure 6.2: The running medians and 1σ scatter of the thick disk (blue), thin disk (red) and bulge (green) trends.

were formed before SNe Ia started to occur. In the bulge, the majority of the stars are old as well, and the enhanced bulge trend could be attributed to its higher metallicity, and potentially, a higher SFR.

Nevertheless, theoretical models in e.g., Kobayashi et al. (2011) cannot reproduce observed Sc trends, and the formation of Sc is still poorly understood. In order to draw any definite conclusions from the abundance trends of Sc, we need to better understand how it is

produced. Potentially, multidimensional models can improve the theoretical yields in the future (Nomoto et al. 2013).

Vanadium

SNe Ia are thought to produce more V than SNe II do (Clayton 2003), but, in fact, little is known about the production of V. Vanadium yields produced in nucleosynthesis models do not show a metallicity dependence, but as in the case of Sc, they reproduce deficient [V/Fe] ratios (e.g., Kobayashi et al. 2011).

Our V trend for the thick disk is enhanced w.r.t. the thin disk by approximately +0.1 dex on average. A similar enhancement of the thick disk is also observed in e.g., Reddy et al. (2006); Adibekyan et al. (2012); Battistini & Bensby (2015). The mean [V/Fe] ratio of the bulge trend is quite similar to the thick disk: the average difference between them is only +0.05 dex. But the trends in Figure 6.1 do not look very similar. The overall disk trend of V has a similar shape as the Sc disk trend, whereas the bulge trend of V appears to be much flatter than the Sc trend.

It is rather difficult to say what the V trend tells us about the evolution and formation of the disk and bulge since this element is not well-explored. From our trend, we can conclude that [V/Fe] shows an enhancement in the bulge compared to the thick and thin disk. However, a significant overlap between the 1σ scatter of the bulge and thick disk trends is present, and it increases with decreasing metallicity.

Chromium

According to some nucleosynthesis computations, chromium does not show any strong variability in SNe II yields and the amount produced in SNe Ia is very similar to the amount of Fe (Kobayashi & Nakasato 2011), resulting in a flat theoretical [Cr/Fe] vs. [Fe/H] trend. As shown in Figure 6.1, the overall disk trend of Cr does agree with the theoretical predictions apart from a slight increase in [Cr/Fe] at supersolar metallicities. This elevation has not been observed in, e.g., Reddy et al. (2006) and Bensby et al. (2014) and may be due to the increasing magnitude of NLTE corrections with decreasing metallicity as discussed in Section 2.3.2. Alternatively, the increase might be caused by any potentially poorly modelled blends that increase with increasing metallicity.

The bulge trend, on the contrary, is non-flat at [Fe/H] $\lesssim 0$ dex and enhanced, but it decreases towards [Cr/Fe] ~ 0 dex at [Fe/H] $\gtrsim 0$ dex. This enhancement can be attributed to the larger scatter in the Cr abundance trend as shown in Figure 5.2. The overlap between

the bulge and disk components is very large.

Due to a large 1σ overlap between the disk and bulge trends and, on average, roughly flat trends, we conclude that Cr is likely to be insensitive to the formation environment. Similar flat Cr trends have been observed for the disk dwarfs and bulge giants in Johnson et al. (2014) as well as for the bulge and disk dwarfs in Bensby et al. (2017).

Manganese

The main production source of Mn is presumed to be SNe Ia which makes it suitable for probing the SNe Ia/SNe II ratio in different systems. Additionally, Mn is also able to provide constraints on properties of progenitor white dwarfs and other mechanisms in SNe Ia (Nomoto et al. 1997; Woosley & Kasen 2011; Yamaguchi et al. 2015).

Our thin and thick disk trends for Mn in Figure 6.1 overlap each other strongly and the running means of the two trends have roughly the same slope at all metallicities. The bulge trend is slightly enhanced compared to the disk components and has a very similar slope. At the lowest metallicities, our bulge trend starts to increase, which we believe is an artificial effect due to a larger scatter.

Many studies on Mn have been carried out, and some of them have found a different behaviour of the thin and thick disks. For example, Feltzing et al. (2007) examined disk dwarfs and concluded that the thick disk stars have a steadily increasing [Mn/Fe] ratio with increasing [Fe/H], whereas the thin disk stars have a flat trend up and until [Fe/H] $\sim$ 0 dex and an increasing trend thereafter. However, Battistini & Bensby (2015), who also worked on disk dwarfs, present a separation that is in agreement with ours: an increasing trend at higher [Fe/H] both in the thin and thick disk (in LTE). Their trend stretches to lower metallicities where it flattens out (see Figure 6.3). Similar results are also presented in Reddy et al. (2006) and Adibekyan et al. (2012). Regarding the bulge, various studies have shown an agreement between Mn abundance trends in the bulge and the overall disk trend (see Figure 11 in McWilliam (2016) and references therein).

Based on the observed increasing [Mn/Fe] ratios with increasing metallicity, Gratton (1989) suggested that Mn might be overproduced in SNe Ia compared to Fe. McWilliam (2016) argues that due to the overproduction of Mn in SNe Ia, one could expect deficient [Mn/Fe] ratios in α-rich systems where the contribution from SNe II has been large, e.g., in the bulge. The trends of Mn in the thick disk would then also be deficient compared to the thin disk, which has only been seen in Battistini & Bensby (2015) when NLTE corrections were applied resulting in a relatively flat overall disk trend. However, while the nucleosynthesis models in Kobayashi & Nakasato (2011) and Nomoto et al. (2013) can reproduce the

observed LTE trends of Mn rather well, they are not able to explain the flat NLTE trend. This indicates that the NLTE corrections might not be correct (as we discussed in Section 2.3.2, the hfs was not taken into account when calculating the corrections) and/or the models might not be complete. In any case, LTE abundances of Mn, as in this work, suggest similar enrichment rates of Mn in the disk and the bulge.

Cobalt

According to the nuclesynthesis model in Kobayashi & Nakasato (2011) and Kobayashi et al. (2011), Co produces a flat trend having similar SNe yields as Cr, which is not supported by the observations. As a possible solution, Kobayashi & Nakasato (2011) suggest that hypernovae[1] (HNe) can solve the issue since they increase Co yields. McWilliam (2016) argues, however, that HNe, apart from producing higher Co abundances in the metal-poor regime, will also result in an underabundant [Cr/Fe] ratio which has not been observed, meaning that HNe do not explain the elevated Co trend.

The [Co/Fe] trend in the thick disk is enhanced by $\sim$+0.1 dex compared to the thin disk, which generally agrees with the findings in Reddy et al. (2006), Adibekyan et al. (2012) and Battistini & Bensby (2015). In the bulge the [Co/Fe] ratio is higher than in the thick disk at comparable metallicities with a significant 1σ overlap between the trends. The enhancement suggests that the thick disk and the bulge have experienced different chemical enrichment paths. Johnson et al. (2014) also note a larger [Co/Fe] ratio in the bulge than in both disk components.

Nickel

SNe Ia have the highest Ni yields but SNe II, being more frequent, result in a comparable total production of Ni (Clayton 2003). This element is known to produce a tight trend since many clean Ni lines are available in the optical region for various stellar types (Jofré et al. 2015).

Our thick disk trend is enhanced in Ni compared to the thin disk by $\sim$ +0.05 dex, which generally agrees with the findings in Reddy et al. (2006) and Adibekyan et al. (2012). The enhancement is small and it matches the overall enhancement of the bulge. If the amount of SNe II nucleosynthesis products is higher in the thick disk and bulge than in the thin disk due to, e.g., a higher SFR, it could explain the overabundances. There is also a significant overlap between the 1σ scatter of the thick disk and bulge trends. Bensby et al. (2017) observe a similar Ni trend in the bulge which falls on top of the thick disk trend.

[1] Hypernovae are very energetic (by a factor of 10 than for a regular SN II) core-collapse supernovae with masses M$\geq$ 20 M$_\odot$ (Kobayashi et al. 2011).

Johnson et al. (2014), on the contrary, find an enhanced Ni trend in the bulge compared to the thick disk at [Fe/H] $\gtrsim$ -0.5.

6.2 Comparison with other works

6.2.1 Solar neighbourhood

We did not find any published results on iron-peak elements in giants in the Solar neighbourhood, where abundances were not determined through an automated pipeline for a large sample of stars, similar to this work. Therefore, in order to check the validity of our results, we compared them to LTE abundances of 714 F and G dwarf and sub-giant stars from the thin and thick disk in Bensby et al. (2014) and Battistini & Bensby (2015). The study in these articles was conducted in a strictly differential analysis w.r.t. the Sun. The authors work on the same spectra and use the same high-precision stellar parameters, because of which these dwarf abundances are also expected to be precise and trustworthy. The comparison is shown in Figure 6.3 and Figure 6.4.

When stars form in a gas cloud they attain different masses, and therefore they evolve on different time scales on the main sequence. Heavier elements, such as the iron-peak group, form during SNe explosions, hence their amounts cannot change in stellar interiors during their lifetimes. Therefore, abundance trends of iron-peak elements should be the same for dwarfs and red giants reflecting the initial chemical composition of the cloud of star-forming gas. In practice, however, trends of measured abundances may not be identical. This depends on many factors. First, it may be due to different model atmospheres used in the analyses, e.g., using plane-parallel models for dwarfs and spherically-symmetric for giants. Second, you may not be able to use the same spectral lines in the analyses because unsaturated unblended lines in dwarf spectra may be saturated and blended in giant spectra. NLTE effects may also affect giants more than dwarfs given lower mass density and, thus, collision rates in giants. If any systematic offsets can be eliminated, observed abundance trends will be similar assuming the precision of the measurements is the same.

For scandium, our [Sc/Fe] values follow the dwarf trend at higher metallicities down to [Fe/H] ~ -0.2 dex. At [Fe/H] $\lesssim -0.2$ our Sc trend starts to increase more rapidly with decreasing metallicity than the one of the dwarfs (see Figure 6.4) and follows the upper envelope of the dwarf [Sc/Fe] ratio, as shown in Figure 6.3.

Our vanadium trend, on the other hand, shows an underabundance at [Fe/H] $\lesssim -0.3$ compared to the dwarfs, as shown in Figure 6.4. At subsolar metallicity and higher, our

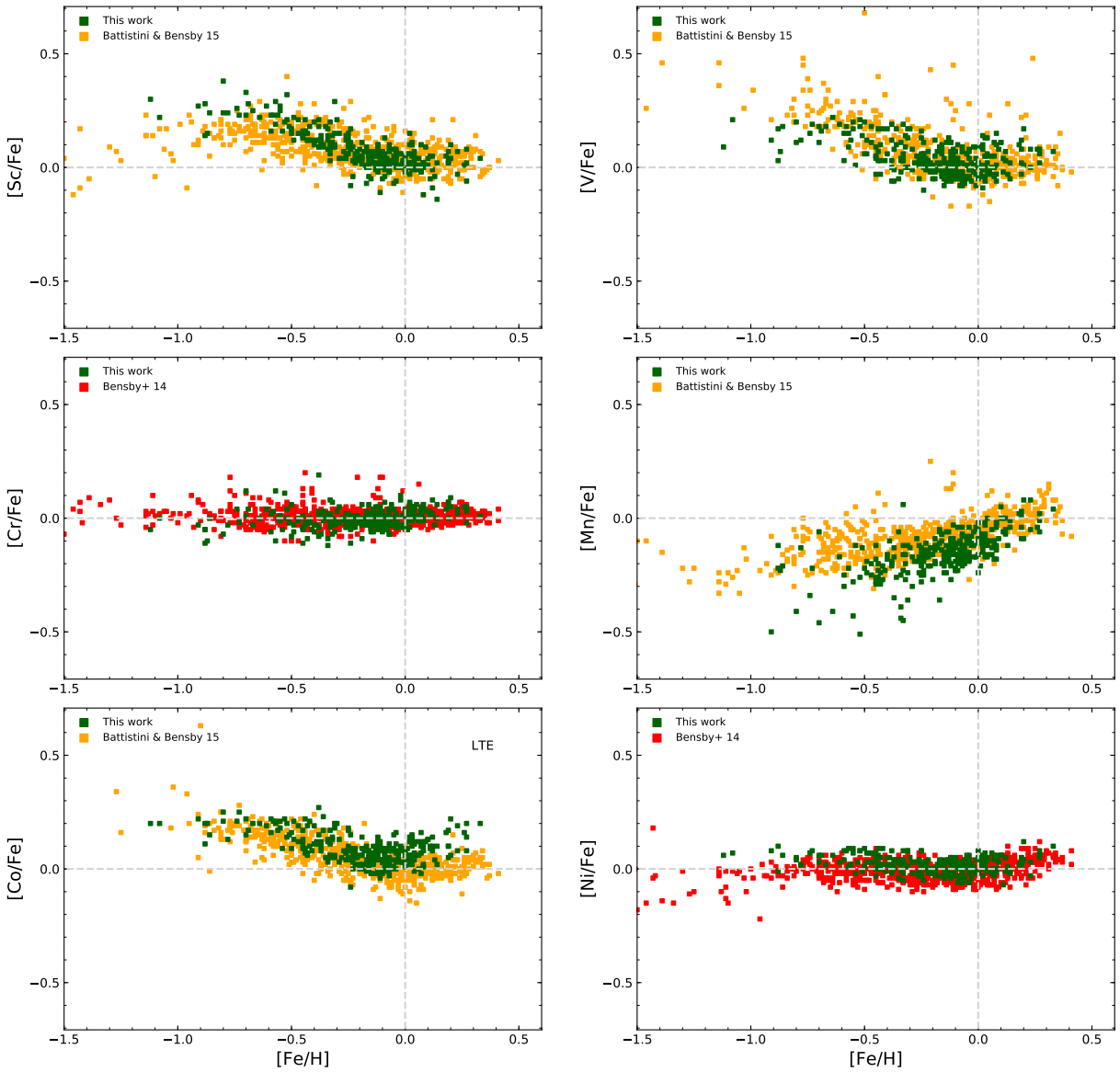

Figure 6.3: [X/Fe] vs. [Fe/H] determined for the disk giants in this work (green) together with the dwarf disk trends from Battistini & Bensby (2015) (orange) and Bensby et al. (2014) (red).

[V/Fe] ratio becomes overabundant instead, and the whole trend seems to be slightly shifted compared to the dwarf values. It is worth mentioning that due to the strictly differential analysis of the dwarfs, our results and the literature trends in Figure 6.3 and 6.4 may not be scaled w.r.t. the same solar abundances, which most probably causes this shift. Otherwise, if the underabundance is ignored, the shapes of both trends show a resemblance.

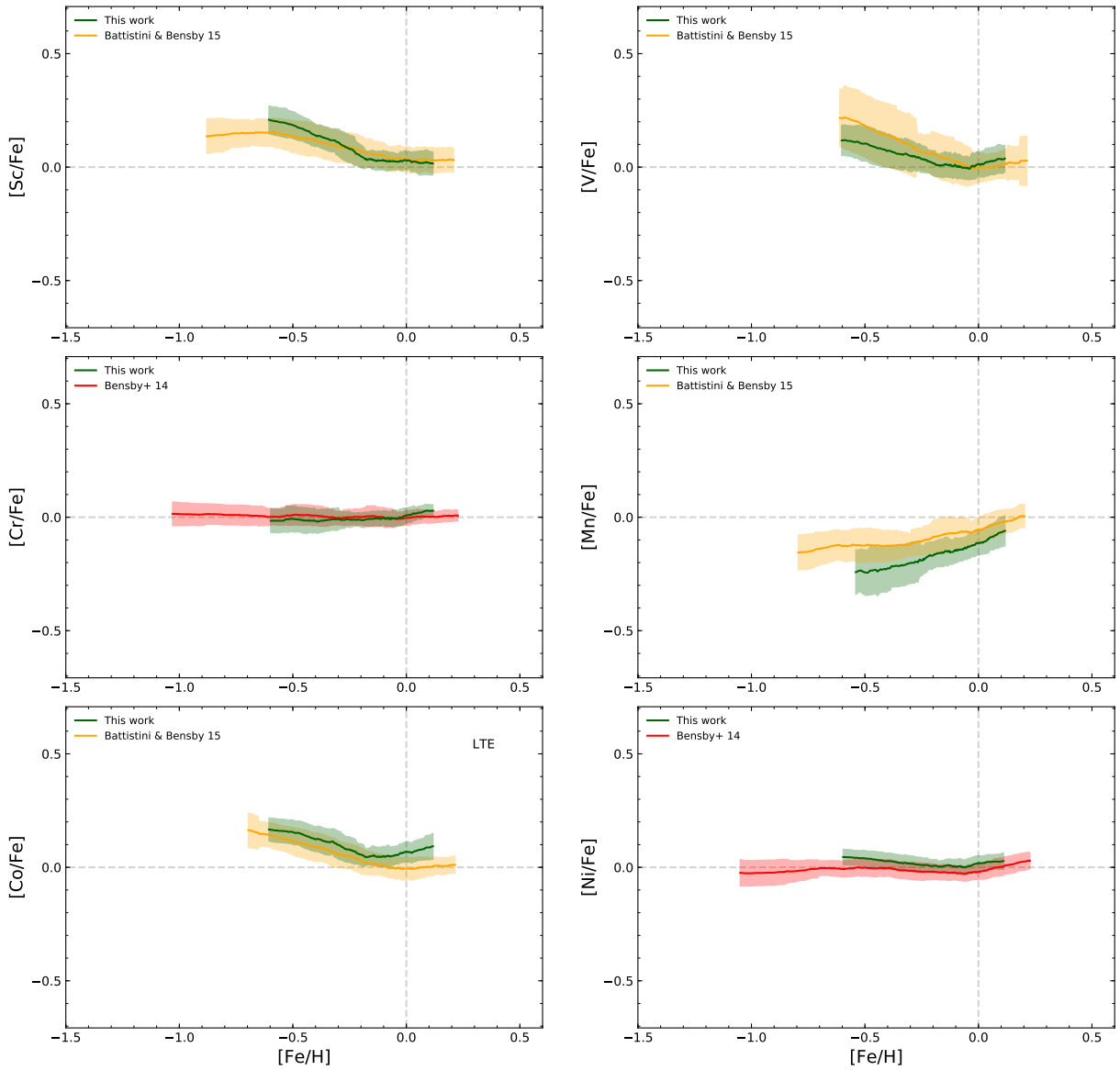

Figure 6.4: Running means and 1σ scatter for the disk samples (thin and thick combined) in Figure 6.3: this work (green), Battistini & Bensby (2015) (orange) and Bensby et al. (2014) (red).

Our [Cr/Fe] ratio shows a similar flat feature as in Bensby et al. (2014), apart from the previously discussed increase at supersolar metallicities. Also, both trends have roughly the same spread.

The manganese trend of giants differs significantly from the results in Battistini & Bensby (2015). At [Fe/H] > 0, the discrepancy is smaller, but as the metallicity decreases, our

trend decreases at a higher rate following the lower envelope of the dwarf trend. Note, that we used only one Mn I line in the analysis which lowers the overall precision. NLTE effects may also be a reasonable explanation of the difference as they might grow with lower metallicities potentially being able to reduce the discrepancy.

In Battistini & Bensby (2015), the [Co/Fe] vs. [Fe/H] trend resembles the trend for Sc, having a plateau at supersolar metallicities followed by an increase with decreasing [Fe/H] which flattens out for [Fe/H] $\lesssim -0.5$. Up to the solar values, our [Co/Fe] vs. [Fe/H] trend follows the literature values, although it is slightly enhanced, which again could be connected to the choice of the solar Co abundance. Notably, at the supersolar metallicities, our [Co/Fe] values show a significant increase up to [Co/Fe] $\sim +0.1$ dex. One of the explanations could be an atomic or molecular contamination, the risk of which increases with higher [Fe/H]. However, all of the four Co I lines used in the analysis show the same feature, hence, line blending is unlikely to explain this upturn. If the continuum has been distorted by molecular pollution instead, then it would have appeared to be lower, resulting in weaker Co I lines, and consequently lower abundances, which is not the case.

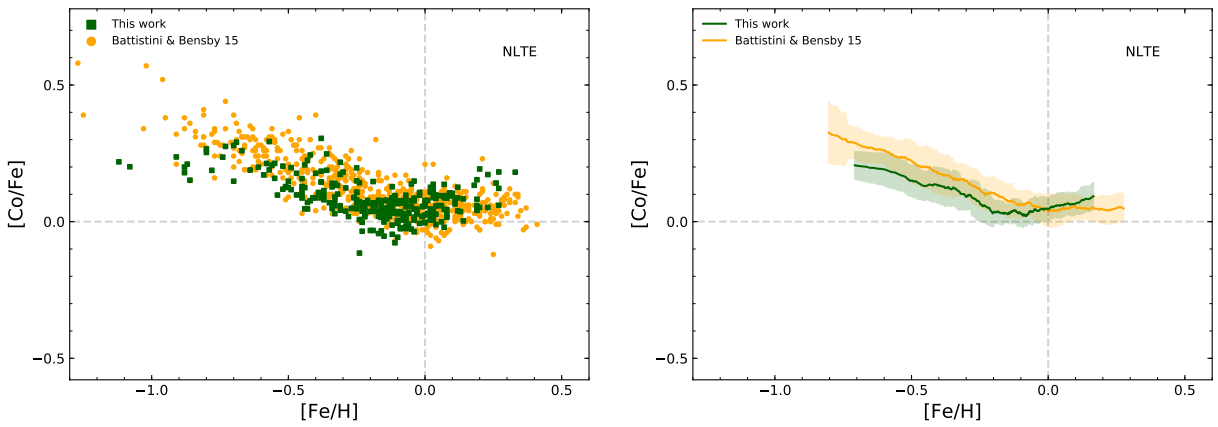

Figure 6.5: Left: the NLTE [Co/Fe] vs. [Fe/H] trends for our disk giants (green) and dwarfs from (Battistini & Bensby 2015) (orange). Right: the running means and 1σ scatter for the trends in the left panel (same colours).

Since NLTE corrections were available for our giants and also the dwarfs in Battistini & Bensby (2015), we can check if NLTE effects can be the reason for the discrepancy. In the left panel in Figure 6.5, we plot the NLTE Co abundances and in the left panel we show the running mean and 1σ scatter of the trends. As for the LTE trend of vanadium, the trends seem to be shifted, which, again, could depend on the solar Co abundance. But most importantly, the NLTE corrections do not reduce our [Co/Fe] ratio at [Fe/H]> 0 sufficiently, or correspondingly increase the ratio in Battistini & Bensby (2015). Given this, we do not understand the origin of this divergence, and the deviation might come

from the model atmospheres, which is difficult to assess.

The [Ni/Fe] vs. [Fe/H] trends show an agreement between our values and those published in Bensby et al. (2014). Our trend is somewhat enhanced as shown in Figure 6.4, this may again be attributed to the solar Ni abundance. Furthermore, the spreads of both trends are similar for the metallicity range of our sample.

6.2.2 Galactic bulge

There are several high-resolution spectroscopic studies of red giants in the bulge that provide abundances of iron-peak elements. Ernandes et al. (2018) have studied 28 red giants in five globular clusters in the bulge and determined abundances of Sc, V and Mn in these stars. Johnson et al. (2014) measured abundances of Cr, Co and Ni in 156 red giants from the Galactic bulge. Schultheis et al. (2017) worked on 269 red giants from the APOGEE survey in the Baade's window (BW) and obtained abundances of Cr, Mn, Co and Ni. Another article on Mn by Barbuy et al. (2013) contains abundances of 56 red giants in the bulge. Moreover, there are 30 stars in our bulge sample that overlap with Barbuy et al. (2013). Finally, Bensby et al. (2017) published abundances of Cr and Ni in 90 F and G dwarfs, turn-off and subgiant stars in the bulge. The location of the aforementioned stars are shown in Figure 4.1, and their abundances are plotted in Figure 6.6 and 6.7. These authors used LTE models, and we also plot our LTE Co trend.

Stars from the globular clusters in Ernandes et al. (2018) stretch down to much lower metallicities, but there is an overlap in [Fe/H] with our most metal-poor giants. For Sc, V and Mn, our results appear more enhanced compared to Ernandes et al. (2018) which is especially clear in Figure 6.7. For Mn, the trend from Ernandes et al. (2018) is lower than all the other literature studies. Moreover, their [V/Fe] ratios in the bulge are comparable to ours in the thin disk. For this reason, it seems likely that the results in Ernandes et al. (2018) suffer from a systematic offset. However, the shapes of their trends are quite similar to ours.

The disk and bulge dwarfs studied in Bensby et al. (2014) and Bensby et al. (2017) appear to have very similar Cr trends predominantly remaining at the solar value over the whole metallicity range as seen in Figure 6.4 and 6.7. Johnson et al. (2014) find a similar flat trend for their RGB stars in the BL and B3 field. Our Cr trend seems enhanced at [Fe/H] < 0 dex, however, as discussed in Section 6.1, this is most probably due to a larger scatter between the individual stars. At [Fe/H] > 0 dex, our trend converges towards [Cr/Fe] $\sim$ 0 dex as well. Interestingly, the trend from Schultheis et al. (2017) changes from flat at [Fe/H] < 0 dex to decreasing at supersolar metallicities.

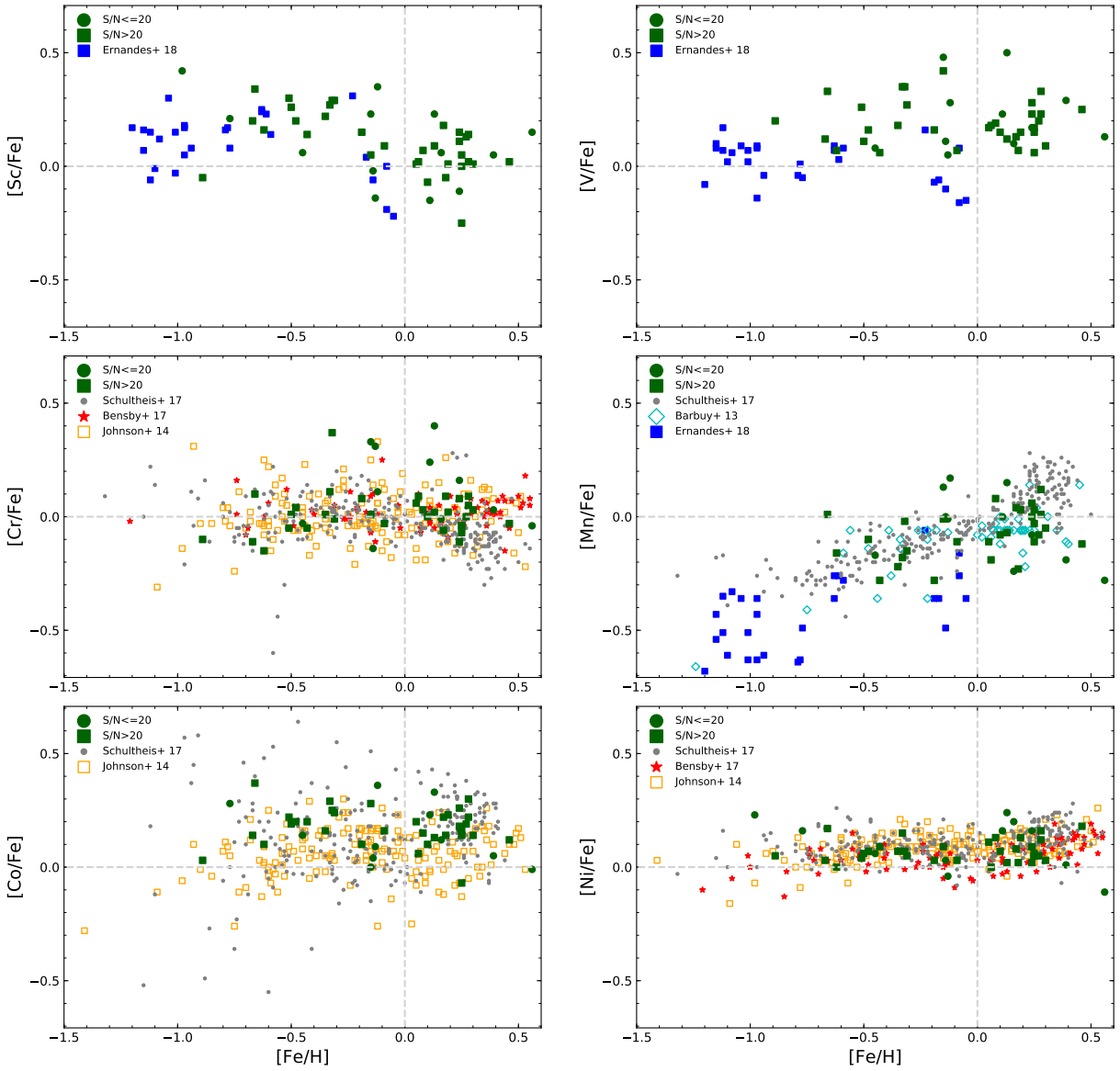

Figure 6.6: [X/Fe] vs. [Fe/H] determined for the bulge giants in this work (green squares for S/N ratios above 20, green circles otherwise) together with the bulge giant trends from Barbuy et al. (2013) (open cyan diamonds), Ernandes et al. (2018) (blue squares), Johnson et al. (2014) (open orange squares) and Schultheis et al. (2017) (gray dots) as well as the microlensed bulge dwarfs from Bensby et al. (2017) (red stars).

As mentioned above, 30 of our stars were the same as the RGB stars from Barbuy et al. (2013). However, as seen in Figure 6.6, even if there are some serious differences in the abundance between the individual stars, the mean value of the discrepancies is only -0.01 dex with the standard deviation of 0.15 dex. For the overlapping stars, Barbuy et al. (2013)

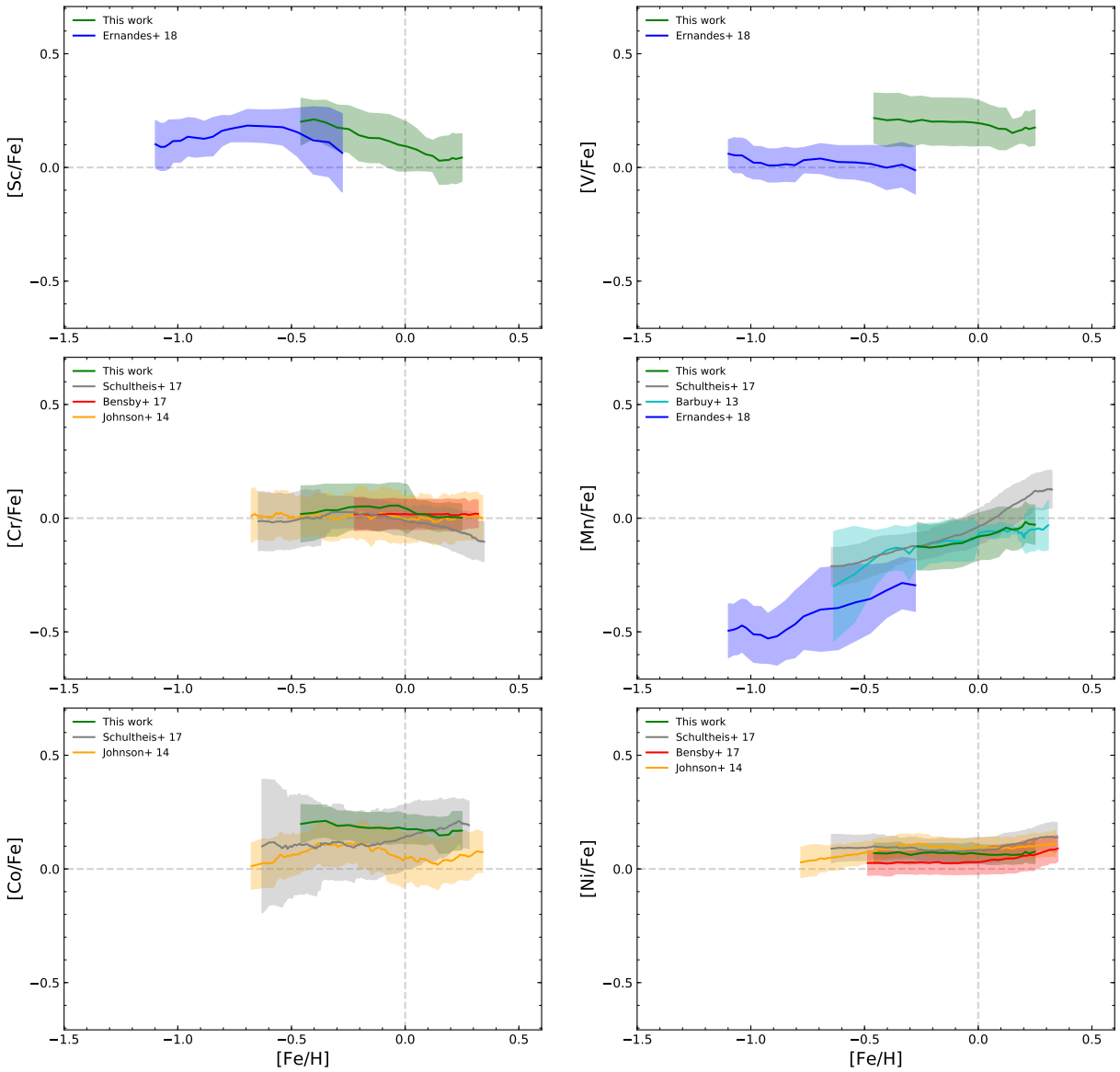

Figure 6.7: Running means and 1σ scatter for the bulge samples in Figure 6.6: this work (green), Barbuy et al. (2013) (cyan), Ernandes et al. (2018) (blue), Johnson et al. (2014) (orange), Schultheis et al. (2017) (gray) and Bensby et al. (2017) (red).

adopted the stellar parameters from Zoccali et al. (2006) and Lecureur et al. (2007), and the latter have been discussed in Jönsson et al. (2017b). They show that the stars with the parameters from Jönsson et al. (2017b) are more spread out along the RGB in the HR-diagram and have a clearer increase in metallicity with decreasing effective temperature than the stars with the parameters from Lecureur et al. (2007) (see Figure 2 in Jönsson et al. 2017b), suggesting that the parameters used here have a higher accuracy and precision. Interestingly, the overall trend in Figure 6.6 and 6.7 is not severely affected by these

differences, which is consistent with the discussion in Section 4.6.2, where we showed that Mn is relatively insensitive to changes in the stellar parameters. Both trends continue to rise at roughly the same rate, whereas the slope of the Mn trend in Schultheis et al. (2017) steepens drastically at supersolar metallicities.

Our Co trend is noticeably flatter than the trends in Johnson et al. (2014) and Schultheis et al. (2017). However, the literature trends do not agree either: at [Fe/H] $\lesssim$ -0.4 dex, the APOGEE trend is flat, whereas the trend in Johnson et al. (2014) is decreasing with decreasing [Fe/H]; at [Fe/H] $\sim$-0.2 the trend from Schultheis et al. (2017) is increasing with increasing [Fe/H], whilst the tend from Johnson et al. (2014) decreases. Finally, at [Fe/H] $\gtrsim$ +0.1 dex the trend from Johnson et al. (2014) starts to increase again. Johnson et al. (2014) find that their Co trend is on average enhanced by $\sim$ +0.14 dex , whilst our trend lies on average at [Co/Fe] = +0.18 dex. The difference between these mean [Co/Fe] ratios is small, but the shapes of the trends vary significantly. It would be interesting to investigate whether a larger stellar sample would change the shape of our trend.

The trends for Ni seem to agree rather well, showing an upward feature at [Fe/H] > 0 dex. The Ni trends of giants are slightly enhanced by $\sim$ +0.05 dex compared to the results in Bensby et al. (2017) which, again, could be a question of the solar Ni abundance.

Comparison summary

In general, we see that our abundance trends of the disk and the bulge mostly show an agreement with the literature, apart from Ernandes et al. (2018). This give us the confidence in our analysis techniques and relevance of the results obtained.

Given this, the observed abundance trends of the examined K giants could be used for theoretical purposes as well. Such trends can work as constraints for Galactic chemical evolution as well as Galaxy formation models where the theoretical outcome of a model needs to be benchmarked against observations.

Chapter 7

Conclusions

Recent observations of the bulge have revealed its boxy/peanut shape, cylindrical stellar rotation and a young stellar population, undoubtedly challenging the idea of its origin. Previously, the Milky Way bulge was thought to be a typical classical bulge formed through dissipation of gas and merging events, whereas now, in the light of the new discoveries, the idea of the secular evolution of the disk has gained more credibility. However, the real picture will almost certainly be more complicated, and apart from the disk stars, the bulge might contain a minor spheroid component. To clarify the picture, observational constraints become highly important, especially in the context of a homogeneous comparative analysis of the disk and bulge.

In this work, we provide such constraints by measuring the abundances of six iron-peak elements (Sc, V, Cr, Mn, Co and Ni) in K giants located in the Solar neighbourhood and the Galactic bulge. Iron-peak elements are produced in thermonuclear and core collapse SNe, and can probe the chemical enrichment path of Galactic components. We use 291 high-resolution optical spectra mainly obtained by the FIES spectrograph at NOT for the disk sample, and 46 spectra of bulge stars collected using the UVES/FLAMES spectrograph at the VLT. To retrieve stellar chemical compositions from the spectra, we use 1-D, spherically-symmetric, hydrostatic, LTE MARCS model atmospheres and a spectral synthesiser SME. The separation of the thick and thin disk components was performed using the Gaussian Mixture Model clustering method. The components were identified according to the [Ti/Fe] ratios and radial velocities of the stars taken from Jönsson et al. (2017a).

The measured abundance trends show that the thick disk is more enhanced in Sc, V, Co and Ni than the thin disk. The bulge, in turn, is even more enhanced in Sc, V and Co than the thick disk. We have not found any results in the literature comparing Sc and V abundances in the disk and bulge, but for Co, Johnson et al. (2014) also observe an enhanced trend of the bulge giants compared to the thick and thin disk dwarfs. The calculated NLTE

corrections are quite small and do not change the trends significantly. Our [Ni/Fe] ratio is very similar in the thick disk and bulge, which is in agreement with the findings in Bensby et al. (2017), which also show a strong overlap between the Ni abundances in these two trends. For Cr, we find very similar trends in all the investigated Galactic components roughly exhibiting solar values throughout the whole metallicity range, suggesting that Cr is not sensitive to the formation environment. This has also been found in Johnson et al. (2014) and Bensby et al. (2017). The trends for Mn obtained here are also very similar in the disk and bulge being steadily increasing with increasing metallicity at about the same rate. This is consistent with the results in, e.g., Barbuy et al. (2013) who compare their bulge giants to the disk dwarfs in Reddy et al. (2006).

While the trends of Cr, Mn and Ni suggest similar chemical enrichment in the bulge and (thick) disk, Sc, Co and especially V exhibit some clear differences. According to the present-day nucleosynthesis models, more Sc is produced with higher metallicity (Woosley & Weaver 1995; Nomoto et al. 2013) and mass (Chieffi & Limongi 2002) of the progenitor star. Given this and the higher average metallicity observed in the bulge, our results would suggest an IMF skewed towards more high-mass stars and/or higher SFR. While the former is expected to be rather similar in the disk and bulge (e.g., Johnson et al. 2014; Bensby et al. 2017), the latter might actually be higher in the bulge, especially considering the higher stellar density in the bulge.

Nevertheless, the nucleosynthesis models cannot reproduce the observed abundance trends of Sc, V and Co in the disk (e.g., Kobayashi et al. 2011; Kobayashi & Nakasato 2011). Without having a clear idea about the production mechanisms of these elements, it is difficult to draw any definite conclusion regarding the chemical enrichment history in the disk and bulge. Moreover, the nucleosynthetic yields should be combined with the other factors, such as the IMF, SFR, gas flows, etc., in order to understand the full picture, which can be done with Galactic chemical evolution models.

Based solely on the observed abundance trends of the examined iron-peak elements, we conclude that the local thick disk and the bulge might not have experienced the same evolutionary path. However, this does not necessarily contradict the fact that the Milky Way bulge is likely to have emerged through dynamical instabilities of the disk. The chemical enrichment history of the *local* thick disk might not be identical to the one of the thick disk region closer to the bulge. A sample of thick disk stars lying closer to the Galactic centre is needed to confirm or reject this conclusion.

Future outlook

A considerable advance of this work would be a larger bulge sample with higher S/N ratio spectra, which would reflect more precisely any potential differences or similarities between the disk and bulge trends. Moreover, assessing an extended wavelength region of the spectra would also be beneficial, allowing the usage of more atomic lines. Additionally, the thick disk sample could be enlarged; especially thick disk stars lying closer to the Galactic centre are of great interest.

With the release of Gaia DR2 at the time of writing, Galactic velocities should have become available, and therefore, all three velocity components could be used when separating the thin and thick disk components. Stellar parallaxes in Gaia DR2 also provide an opportunity to check the precision of the surface gravities measured in Jönsson et al. (2017a,b).

Bibliography

Abadi, M. G., Navarro, J. F., Steinmetz, M., & Eke, V. R. 2003, ApJ, 591, 499

Adibekyan, V. Z., Santos, N. C., Sousa, S. G., & Israelian, G. 2011, A&A, 535, L11

Adibekyan, V. Z., Sousa, S. G., Santos, N. C., et al. 2012, A&A, 545, A32

Athanassoula, E. 2005, MNRAS, 358, 1477

Babusiaux, C., Gómez, A., Hill, V., et al. 2010, A&A, 519, A77

Barbuy, B., Chiappini, C., & Gerhard, O. 2018, ArXiv e-prints

Barbuy, B., Hill, V., Zoccali, M., et al. 2013, A&A, 559, A5

Battistini, C. & Bensby, T. 2015, A&A, 577, A9

Bensby, T., Feltzing, S., Gould, A., et al. 2017, A&A, 605, A89

Bensby, T., Feltzing, S., & Oey, M. S. 2014, A&A, 562, A71

Bensby, T., Zenn, A. R., Oey, M. S., & Feltzing, S. 2007, ApJ, 663, L13

Bergemann, M. & Cescutti, G. 2010, A&A, 522, A9

Bergemann, M. & Gehren, T. 2008, A&A, 492, 823

Bergemann, M. & Nordlander, T. 2014, ArXiv e-prints

Bergemann, M., Pickering, J. C., & Gehren, T. 2010, MNRAS, 401, 1334

Blackwell-Whitehead, R. & Bergemann, M. 2007, A&A, 472, L43

Bland-Hawthorn, J. & Gerhard, O. 2016, ARA&A, 54, 529

Cardelli, J. A., Clayton, G. C., & Mathis, J. S. 1989, ApJ, 345, 245

Cardon, B. L., Smith, P. L., Scalo, J. M., Testerman, L., & Whaling, W. 1982, ApJ, 260, 395

Chaplin, W. J. & Miglio, A. 2013, ARA&A, 51, 353

Chiappini, C., Matteucci, F., & Gratton, R. 1997, ApJ, 477, 765

Chieffi, A. & Limongi, M. 2002, ApJ, 577, 281

Clarkson, W. I., Sahu, K. C., Anderson, J., et al. 2011, ApJ, 735, 37

Clayton, D. 2003, Handbook of Isotopes in the Cosmos, 326

Combes, F. & Sanders, R. H. 1981, A&A, 96, 164

Di Matteo, P., Haywood, M., Gómez, A., et al. 2014, A&A, 567, A122

Ducati, J. R. 2002, VizieR Online Data Catalog, 2237

Eggen, O. J., Lynden-Bell, D., & Sandage, A. R. 1962, ApJ, 136, 748

Ernandes, H., Barbuy, B., Alves-Brito, A., et al. 2018, ArXiv e-prints

Feltzing, S., Fohlman, M., & Bensby, T. 2007, A&A, 467, 665

Gillessen, S., Eisenhauer, F., Trippe, S., et al. 2009, ApJ, 692, 1075

Gonzalez, O. A. & Gadotti, D. 2016, in Astrophysics and Space Science Library, Vol. 418, Galactic Bulges, ed. E. Laurikainen, R. Peletier, & D. Gadotti, 199

Gonzalez, O. A., Rejkuba, M., Zoccali, M., Valenti, E., & Minniti, D. 2011, A&A, 534, A3

Gonzalez, O. A., Rejkuba, M., Zoccali, M., et al. 2012, A&A, 543, A13

Gratton, R. G. 1989, A&A, 208, 171

Grevesse, N., Asplund, M., & Sauval, A. J. 2007, Space Sci. Rev., 130, 105

Gustafsson, B., Edvardsson, B., Eriksson, K., et al. 2008, A&A, 486, 951

Heiter, U., Lind, K., Asplund, M., et al. 2015, Phys. Scr, 90, 054010

Henry, R. B. C. & Worthey, G. 1999, PASP, 111, 919

Hill, V., Lecureur, A., Gómez, A., et al. 2011, A&A, 534, A80

Hinkle, K., Wallace, L., Valenti, J., & Harmer, D. 2000, Visible and Near Infrared Atlas of the Arcturus Spectrum 3727-9300 A

Jofré, P., Heiter, U., Soubiran, C., et al. 2015, A&A, 582, A81

Jofré, P., Heiter, U., Soubiran, C., et al. 2014, A&A, 564, A133

Johnson, C. I., Rich, R. M., Kobayashi, C., Kunder, A., & Koch, A. 2014, AJ, 148, 67

Johnson, D. R. H. & Soderblom, D. R. 1987, AJ, 93, 864

Johnson, J. A. 2002, ApJS, 139, 219

Jönsson, H., Ryde, N., Nordlander, T., et al. 2017a, A&A, 598, A100

Jönsson, H., Ryde, N., Schultheis, M., & Zoccali, M. 2017b, A&A, 598, A101

Jordan, G. C., Gupta, S. S., & Meyer, B. S. 2003, Phys. Rev. C, 68, 065801

Klement, R. J. 2010, The Astronomy and Astrophysics Review, 18, 567

Kobayashi, C. & Arimoto, N. 1999, ApJ, 527, 573

Kobayashi, C., Karakas, A. I., & Umeda, H. 2011, MNRAS, 414, 3231

Kobayashi, C. & Nakasato, N. 2011, ApJ, 729, 16

Kobayashi, C., Umeda, H., Nomoto, K., Tominaga, N., & Ohkubo, T. 2006, ApJ, 653, 1145

Kormendy, J. 2016, in Astrophysics and Space Science Library, Vol. 418, Galactic Bulges, ed. E. Laurikainen, R. Peletier, & D. Gadotti, 431

Kormendy, J. & Kennicutt, Jr., R. C. 2004a, ARA&A, 42, 603

Kormendy, J. & Kennicutt, Jr., R. C. 2004b, ARA&A, 42, 603

Kunder, A., Koch, A., Rich, R. M., et al. 2012, AJ, 143, 57

Kupka, F., Piskunov, N., Ryabchikova, T. A., Stempels, H. C., & Weiss, W. W. 1999, A&AS, 138, 119

Kurucz, R. L. 2009, Robert L. Kurucz on-line database of observed and predicted atomic transitions

Kurucz, R. L. 2010, Robert L. Kurucz on-line database of observed and predicted atomic transitions

Lagarde, N., Miglio, A., Eggenberger, P., et al. 2015, A&A, 580, A141

Lai, D. K., Bolte, M., Johnson, J. A., et al. 2008, ApJ, 681, 1524

Lawler, J. E. & Dakin, J. T. 1989, Journal of the Optical Society of America B Optical Physics, 6, 1457, (LD)

Lecureur, A., Hill, V., Zoccali, M., et al. 2007, A&A, 465, 799

Lind, K., Bergemann, M., & Asplund, M. 2012, MNRAS, 427, 50

Lodders, K. 2010, in Principles and Perspectives in Cosmochemistry, ed. A. Goswami & B. E. Reddy (Berlin, Heidelberg: Springer Berlin Heidelberg), 379–417

Lütticke, R., Dettmar, R.-J., & Pohlen, M. 2000, A&AS, 145, 405

Marigo, P., Girardi, L., Bressan, A., et al. 2017, ApJ, 835, 77

Martig, M., Fouesneau, M., Rix, H.-W., et al. 2016, MNRAS, 456, 3655

Martinez-Valpuesta, I., Shlosman, I., & Heller, C. 2006, ApJ, 637, 214

Matteucci, F. 2012, Chemical Evolution of Galaxies

McMillan, P. J. 2011, MNRAS, 414, 2446

McWilliam, A. 1997, ARA&A, 35, 503

McWilliam, A. 2016, PASA, 33, e040

McWilliam, A. & Zoccali, M. 2010, ApJ, 724, 1491

Meléndez, J., Asplund, M., Alves-Brito, A., et al. 2008, A&A, 484, L21

Micali, A., Matteucci, F., & Romano, D. 2013, MNRAS, 436, 1648

Mikolaitis, Š., de Laverny, P., Recio-Blanco, A., et al. 2017, A&A, 600, A22

Nataf, D. M., Udalski, A., Gould, A., Fouqué, P., & Stanek, K. Z. 2010, ApJ, 721, L28

Ness, M., Freeman, K., Athanassoula, E., et al. 2013a, MNRAS, 430, 836

Ness, M., Freeman, K., Athanassoula, E., et al. 2013b, MNRAS, 432, 2092

Ness, M., Hogg, D. W., Rix, H.-W., et al. 2016, The Astrophysical Journal, 823, 114

Nomoto, K., Iwamoto, K., Nakasato, N., et al. 1997, Nuclear Physics A, 621, 467

Nomoto, K., Kobayashi, C., & Tominaga, N. 2013, ARA&A, 51, 457

Nordlander, T. 2017, Galactic archaeology with metal-poor stars (Uppsala: Acta Universitatis Upsaliensis), diss. (sammanfattning) Uppsala : Uppsala universitet, 2017

Pakhomov, Y., Piskunov, N., & Ryabchikova, T. 2017, in Astronomical Society of the Pacific Conference Series, Vol. 510, Stars: From Collapse to Collapse, ed. Y. Y. Balega, D. O. Kudryavtsev, I. I. Romanyuk, & I. A. Yakunin, 518

Pedregosa, F., Varoquaux, G., Gramfort, A., et al. 2011, Journal of Machine Learning Research

Pehlivan Rhodin, A., Belmonte, M. T., Engström, L., et al. 2017, MNRAS, 472, 3337

Petit, P., Louge, T., Théado, S., et al. 2014, PASP, 126, 469

Pipino, A. & Matteucci, F. 2008, in The Metal-Rich Universe, ed. G. Israelian & G. Meynet, 270

Piskunov, N. & Valenti, J. A. 2017, A&A, 597, A16

Prochaska, J. X. & McWilliam, A. 2000, ApJ, 537, L57

Reddy, B. E., Lambert, D. L., & Allende Prieto, C. 2006, MNRAS, 367, 1329

Rich, R. M., Origlia, L., & Valenti, E. 2012, ApJ, 746, 59

Rich, R. M., Ryde, N., Thorsbro, B., et al. 2017, AJ, 154, 239

Rutten, R. J. 2003, Radiative Transfer in Stellar Atmospheres

Ryde, N., Fritz, T. K., Rich, R. M., et al. 2016, ApJ, 831, 40

Scannapieco, C. & Tissera, P. B. 2003, MNRAS, 338, 880

Schneider, P. 2015, Extragalactic Astronomy and Cosmology: An Introduction

Schultheis, M., Rojas-Arriagada, A., García Pérez, A. E., et al. 2017, A&A, 600, A14

Schultheis, M., Ryde, N., & Nandakumar, G. 2016, A&A, 590, A6

Scott, P., Asplund, M., Grevesse, N., Bergemann, M., & Sauval, A. J. 2015, A&A, 573, A26

Shen, J., Rich, R. M., Kormendy, J., et al. 2010, ApJ, 720, L72

Sobeck, J. S., Lawler, J. E., & Sneden, C. 2007, ApJ, 667, 1267

Thygesen, A. O., Frandsen, S., Bruntt, H., et al. 2012, A&A, 543, A160

Valenti, E., Zoccali, M., Gonzalez, O. A., et al. 2016, A&A, 587, L6

Valenti, J. A. & Piskunov, N. 1996, A&AS, 118, 595

van Loon, J. T., Gilmore, G. F., Omont, A., et al. 2003, MNRAS, 338, 857

Vásquez, S., Zoccali, M., Hill, V., et al. 2013, A&A, 555, A91

Wegg, C. & Gerhard, O. 2013, MNRAS, 435, 1874

Weiland, J. L., Arendt, R. G., Berriman, G. B., et al. 1994, ApJ, 425, L81

Whaling, W., Hannaford, P., Lowe, R. M., Biemont, E., & Grevesse, N. 1985, A&A, 153, 109

Wood, M. P., Lawler, J. E., Sneden, C., & Cowan, J. J. 2014, ApJS, 211, 20

Woosley, S. E. & Kasen, D. 2011, ApJ, 734, 38

Woosley, S. E. & Weaver, T. A. 1995, ApJS, 101, 181

Yamaguchi, H., Badenes, C., Foster, A. R., et al. 2015, ApJ, 801, L31

Zhang, H. W., Gehren, T., & Zhao, G. 2008, A&A, 481, 489

Zoccali, M., Lecureur, A., Barbuy, B., et al. 2006, A&A, 457, L1

Appendix A

Atomic data for spectral lines used

Table A.1: Atomic lines used in the analysis. The elements and excitation states are given in column 1, the transition wavelength is shown in column 2, $\log gf$ values are listed in column 3. The energy of the lower transition level is given in column 4. Finally, column 5 specifies the reference for the $\log gf$-values.

Element	Wavelength [Å]	$\log gf$	E_{exc}^{low} [eV]	Reference
Sc II	6245.6205	-1.624	1.50695	Kurucz (2009)
Sc II	6245.6290	-2.364	1.50695	Kurucz (2009)
Sc II	6245.6309	-1.795	1.50695	Kurucz (2009)
Sc II	6245.6362	-3.364	1.50695	Kurucz (2009)
Sc II	6245.6380	-2.181	1.50695	Kurucz (2009)
Sc II	6245.6396	-2.002	1.50695	Kurucz (2009)
Sc II	6245.6438	-2.946	1.50695	Kurucz (2009)
Sc II	6245.6454	-2.148	1.50695	Kurucz (2009)
Sc II	6245.6468	-2.273	1.50695	Kurucz (2009)
Sc II	6245.6499	-2.712	1.50695	Kurucz (2009)
Sc II	6245.6513	-2.207	1.50695	Kurucz (2009)
Sc II	6245.6523	-2.691	1.50695	Kurucz (2009)
Sc II	6245.6544	-2.566	1.50695	Kurucz (2009)
Sc II	6245.6555	-2.390	1.50695	Kurucz (2009)
Sc II	6245.6573	-2.469	1.50695	Kurucz (2009)
Sc II	6300.6835	-2.524	1.50695	Kurucz (2009)
Sc II	6300.6854	-3.094	1.50695	Kurucz (2009)

continued Table A.1

Element	Wavelength [Å]	$\log gf$	E_{exc}^{low} [eV]	Reference
Sc II	6300.6927	-3.094	1.50695	Kurucz (2009)
Sc II	6300.6946	-2.922	1.50695	Kurucz (2009)
Sc II	6300.6963	-2.936	1.50695	Kurucz (2009)
Sc II	6300.7020	-2.936	1.50695	Kurucz (2009)
Sc II	6300.7037	-3.618	1.50695	Kurucz (2009)
Sc II	6300.7051	-2.947	1.50695	Kurucz (2009)
Sc II	6300.7095	-2.947	1.50695	Kurucz (2009)
Sc II	6300.7109	-5.044	1.50695	Kurucz (2009)
Sc II	6300.7119	-3.120	1.50695	Kurucz (2009)
Sc II	6300.7150	-3.120	1.50695	Kurucz (2009)
Sc II	6300.7160	-3.296	1.50695	Kurucz (2009)
Sc II	6320.8320	-2.410	1.5003	Kurucz (2009)
Sc II	6320.8386	-2.606	1.5003	Kurucz (2009)
Sc II	6320.8503	-2.606	1.5003	Kurucz (2009)
Sc II	6320.8569	-3.791	1.5003	Kurucz (2009)
Sc II	6320.8617	-2.610	1.5003	Kurucz (2009)
Sc II	6320.8711	-2.610	1.5003	Kurucz (2009)
Sc II	6320.8759	-2.865	1.5003	Kurucz (2009)
Sc II	6604.5822	-2.505	1.35695	Lawler & Dakin (1989)
Sc II	6604.5898	-2.347	1.35695	Lawler & Dakin (1989)
Sc II	6604.5942	-1.935	1.35695	Lawler & Dakin (1989)
Sc II	6604.5964	-2.358	1.35695	Lawler & Dakin (1989)
Sc II	6604.5996	-2.333	1.35695	Lawler & Dakin (1989)
Sc II	6604.6019	-2.531	1.35695	Lawler & Dakin (1989)
Sc II	6604.6039	-3.029	1.35695	Lawler & Dakin (1989)
Sc II	6604.6073	-4.455	1.35695	Lawler & Dakin (1989)
Sc II	6604.6096	-2.707	1.35695	Lawler & Dakin (1989)
Sc II	6604.6116	-2.505	1.35695	Lawler & Dakin (1989)
Sc II	6604.6137	-2.347	1.35695	Lawler & Dakin (1989)
Sc II	6604.6148	-2.358	1.35695	Lawler & Dakin (1989)
Sc II	6604.6150	-2.531	1.35695	Lawler & Dakin (1989)

continued Table A.1

Element	Wavelength [Å]	$\log gf$	E_{exc}^{low} [eV]	Reference
V I	6002.28170	-2.2850	1.2180	Whaling et al. (1985)
V I	6002.29380	-2.1600	1.2180	Whaling et al. (1985)
V I	6002.30700	-2.3470	1.2180	Whaling et al. (1985)
V I	6256.83910	-3.3560	0.2750	Whaling et al. (1985)
V I	6256.85670	-3.1740	0.2750	Whaling et al. (1985)
V I	6256.87060	-2.5340	0.2750	Whaling et al. (1985)
V I	6256.88380	-2.7580	0.2750	Whaling et al. (1985)
V I	6256.89540	-3.0370	0.2750	Whaling et al. (1985)
V I	6256.91370	-2.6120	0.2750	Whaling et al. (1985)
V I	6256.92120	-3.2080	0.2750	Whaling et al. (1985)
V I	6531.39930	-1.3450	1.2180	Whaling et al. (1985)
V I	6531.41380	-1.2200	1.2180	Whaling et al. (1985)
V I	6531.42920	-1.4080	1.2180	Whaling et al. (1985)
V I	6565.87800	-2.0700	1.1830	Whaling et al. (1985)
Cr I	5844.59500	-1.7700	3.0130	Sobeck et al. (2007)
Cr I	6630.01000	-3.5600	1.0300	Kurucz (2010)
Mn I	6440.91040	-1.8610	3.7720	Blackwell-Whitehead & Bergemann (2007)
Mn I	6440.92260	-1.7700	3.7720	Blackwell-Whitehead & Bergemann (2007)
Mn I	6440.93220	-2.5200	3.7720	Blackwell-Whitehead & Bergemann (2007)
Mn I	6440.94450	-1.4900	3.7720	Blackwell-Whitehead & Bergemann (2007)
Mn I	6440.95770	-2.5200	3.7720	Blackwell-Whitehead & Bergemann (2007)
Co I	6004.97710	-5.3790	1.7100	Cardon et al. (1982)
Co I	6004.98780	-4.5130	1.7100	Cardon et al. (1982)
Co I	6005.00050	-3.8880	1.7100	Cardon et al. (1982)
Co I	6005.01480	-4.2550	1.7100	Cardon et al. (1982)
Co I	6005.03710	-3.8470	1.7100	Cardon et al. (1982)
Co I	6005.05890	-3.9960	1.7100	Cardon et al. (1982)
Co I	6005.07030	-4.8260	1.7100	Cardon et al. (1982)
Co I	6116.95670	-3.1420	1.7850	Cardon et al. (1982)
Co I	6116.99400	-2.6950	1.7850	Cardon et al. (1982)
Co I	6117.03320	-3.4730	1.7850	Cardon et al. (1982)

continued Table A.1

Element	Wavelength [Å]	$\log gf$	E_{exc}^{low} [eV]	Reference
Co I	6188.92480	-3.7950	1.7100	Cardon et al. (1982)
Co I	6188.93830	-3.0960	1.7100	Cardon et al. (1982)
Co I	6188.96680	-3.6140	1.7100	Cardon et al. (1982)
Co I	6188.97810	-3.3880	1.7100	Cardon et al. (1982)
Co I	6188.99160	-3.7950	1.7100	Cardon et al. (1982)
Co I	6189.00470	-3.3750	1.7100	Cardon et al. (1982)
Co I	6189.02860	-3.3020	1.7100	Cardon et al. (1982)
Co I	6189.05060	-3.3920	1.7100	Cardon et al. (1982)
Co I	6189.06980	-3.3500	1.7100	Cardon et al. (1982)
Co I	6632.40640	-2.5680	2.2800	Cardon et al. (1982)
Co I	6632.42120	-2.7830	2.2800	Cardon et al. (1982)
Co I	6632.43590	-3.0660	2.2800	Cardon et al. (1982)
Co I	6632.45050	-2.7260	2.2800	Cardon et al. (1982)
Co I	6632.46720	-2.8140	2.2800	Cardon et al. (1982)
Co I	6632.48310	-2.8660	2.2800	Cardon et al. (1982)
Ni I	6007.30980	-3.4000	1.6760	Wood et al. (2014)
Ni I	6177.24150	-3.4600	1.8260	Wood et al. (2014)
Ni I	6223.98100	-0.9100	4.1050	Wood et al. (2014)
Ni I	6378.24700	-0.8200	4.1540	Wood et al. (2014)